A Thesis

entitled

Analysis of Coincident HICO and Airborne Hyperspectral Images Over Lake Erie Western Basin HABs

by

Michael T. Cline Jr.

Submitted to the Graduate Faculty as partial fulfillment of the requirements for the

Master of Science Degree in

Geology

Dr. Richard Becker, Committee Chair

Dr. Thomas Bridgeman, Committee Member

Dr. Kevin Czajkowski, Committee Member

Dr. Amanda Bryant-Friedrich, Dean
College of Graduate Studies

The University of Toledo

August 2016

An Abstract of

Analysis of Coincident HICO and Airborne Hyperspectral Images Over Lake Erie Western Basin HABs

by

Michael T. Cline Jr.

Submitted to the Graduate Faculty as partial fulfillment of the requirements for the
Master of Science Degree in
Geology

The University of Toledo

August 2016

Harmful algal blooms (HABs) produce waterborne toxins that pose a significant threat to people, livestock, and wildlife. Nearly 40 million people in both Canada and the U.S. depend on Great Lakes water. In the summer of 2014, in the Lake Erie Western Basin, an HAB of the cyanobacteria Microcystis was so severe that a do-not-drink advisory was in effect for the greater Toledo area, Ohio. This advisory applied to the water supply to over 400,000 people from a single water intake. Bloom intensity, composition, and spatial variability were investigated by comparing coincidental hyperspectral data from NASA's HICO, and NASA GRC's HSI airborne sensor, with on-lake ASD radiometer measurements and in situ water quality testing as ground reference data. Coincident data sets were obtained with HICO only on one day in 2014, however all other datasets coincide four times in 2015. Remote sensing data were atmospherically corrected using the empirical line method, utilizing dark reference spectra from a nearby asphalt parking lot measured from ASD and HSI radiometers. Cyanobacteria Index (CI) images were created from processed images using the Wynne (2010) algorithm, previously used for MODIS and MERIS imagery. This algorithm-generated CI images provide reliable results for both ground level (R^2=0.921), airborne (R^2=0.7981), and satellite imagery (R^2=0.7794) for seven sampling points. The ability to robustly atmospherically correct and generate useful CI maps from airborne and satellite sensors can provide a time- and cost-effective method for HABs analysis. Timely processing of these high spatial and spectral resolution remote sensing data can aid in management of water intake resources. These results will help to improve methods leading to HABs mapping by testing different algal retrieval algorithms and atmospheric correction techniques using a three tiered hyperspectral sensor approach utilizing satellite, airborne, and ground level sensors, coupled with water quality measurements as reference data.

The world's biggest "Thank you" goes out to my parents for supporting me in everything that I do. Their support comes unconditionally, whether it be financially (especially this one) or emotionally. I can always count on them for advice, support, to lend an ear, and even help me move! Thank you Keelie and Mike Cline, to the best parents anyone could ask for, I love you both.

Acknowledgements

A tremendous “Thank you” is owed to Dr. Richard Becker, my undergraduate and graduate advisor. Without his expertise, patience, reliability, and general good personality, none of this research could have been possible. Over the last few years he and I have spent a lot of time together; in the lab, on the lake, in classrooms, and even abroad on class trips and conferences, from all this I only have good things to say. Thank you again, Dr. Becker, I am very fortunate to call him my advisor and friend.

Thank you to Dr. Thomas Bridgeman and his lab for providing lake measurements used in this research and for showing me the ways of the Lake. Without Dr. Bridgeman’s data, this research would not have been possible.

Thank you to Dr. Kevin Czajkowski, for providing further insight into the world of remote sensing, while also helping to edit this thesis.

Thank you to NASA Glenn Research Center’s Hyperspectral Observation of Harmful Algal Blooms Project, the Center for Advancement of Science in Space (CASIS), and the Ohio Department of Higher Education for funding this research.

Table of Contents

List of Tables

List of Figures

List of Abbreviations

6Sv	Second Simulation of a Satellite Signal in the Solar Spectrum
AOP	Apparent Optical Property
ASD	Analytic Spectral Devices, inc.
CDOM	Colored Dissolved Organic Matter
CI	Cyanobacterial Index
CPA-A	Color Producing Agent Algorithm
ELM	Empirical Line Method
EM	Electromagnetic (Radiation)
ERIM	Environmental Research Institute of Michigan
FOV	Field of View
GRC	Glenn Research Center
HABs	Harmful Algal Blooms
HICO	Hyperspectral Imager of the Coastal Ocean
HSI	Hyperspectral Instrument
IOP	Inherent Optical Properties
ISS	International Space Station
ISOC-HAB	International Symposium on Cyanobacterial Harmful Algal Blooms
MERIS	Medium Resolution Imaging Spectrometer
MODIS	Moderate Resolution Imaging Spectrometer
MSS	Multispectral Sensor
NASA	National Aeronautics and Space Administration
NOAA	National Oceanic and Atmospheric Administration
NTU	Nephelometric Turbidity Units
SM	Suspended Minerals
TSS	Total Suspended Solids

UV	Ultraviolet
WLE	Western Lake Erie
WLELL	Western Lake Erie Limnology Laboratory

List of Symbols

Δr	Thickness of water column
Δv	Volume of water
λ	Wavelength. 681 nm or MERIS band 8.
λ^+	709 nm or MERIS band 9
λ^-	665 nm or MERIS band 7
σ	Cross-sectional area of backscatter
Φ_a	Coefficient of absorption
Φ_i	Coefficient of incident radiation
Φs	Coefficient of scattering
Φt	Coefficient of transmittance
a	Coefficient of absorption
a_i	Coefficient of absorption at wavelength i
a*PC(λ)	Absorption coefficient of Phycocyanin at wavelength λ
b	Coefficient of backscattering
b_i	Coefficient of backscattering at wavelength i
C	Concentration
L_v	Water leaving radiance
R	Reflectance
R_{rs}	Remote sensing reflectance
W	Concentration of pure water

Chapter 1

Introduction and Hypothesis

1.1 Introduction

Nearly 40 million people depend on fresh water from the North American Great Lakes for both consumption and recreational usage. Lake Erie is the most productive of all the Great Lakes in terms of both commercial harvest, and recreational fishing usage. Roughly 61% of all commercial fish from the Great Lakes are harvested from Lake Erie, and 37% of all recreational fishing is done on Lake Erie (MichiganSeaGrant, 2006). Approximately 12.5 million people live within the Lake Erie basin, and depend on it as a source of drinking water (MichiganSeaGrant, 2006). While Lake Erie is the most productive of the Great Lakes, it is also the most susceptible to the adverse effects of harmful algal blooms (HABs). HABs pose a significant threat to Lake Erie's Western Basin as its warm, shallow waters are influenced heavily by sediment and nutrient input from the Maumee River watershed. Current analysis of HABs requires intensive field work, necessitating significant time and money. Hyperspectral analysis of HABs, using *in situ* ASD, NASA HICO, and NASA HSI sensors can provide a spatially extensive cost- and time-effective analysis of both extent and make-up of HABs in the Lake Erie western basin.

1.2 Statement of Problem

Lake Erie is the shallowest of the Great Lakes with a maximum depth of just 64 meters, with a western basin depth of 7.4 meters; while also having the lowest water volume (CGLP, 1977). The shallow nature of Western Lake Erie (WLE) makes it prone to algal blooms due to an influx of sediment rich water from the Maumee River containing agricultural runoff containing of phosphorous and nitrate. WLE blooms are typically composed of *Microcystis spp.,* which produce the toxin microcystin. Microcystin is a hepatotoxin which can cause acute liver failure, nausea, muscle weakness, visual disturbances, and skin irritation (Azevedo et al., 2002). The most notable case of microcystin poisoning occurred in 1996 in Caruaru, Brazil with 116 documented patients, of which 100 experienced acute liver failure (Azevedo et al., 2002). Though there have not been any severe microcystin poisonings in the Great Lakes region, HABs have proven to be an annual problem to WLE (Bridgeman et al., 2013), as well as in the other Great Lakes. Lake Erie *Microcystis* blooms have been increasing in size since the 1990s (Michalak et al., 2013). Of significant note, in August of 2014, the WLE HAB was so intense that the city of Toledo, Ohio was placed under a do-not-drink advisory. Concentrations of microcystin in WLE have been observed to surpass 20 µg L^{-1} while the World Health Organization provides a baseline limit of 1 µg L^{-1} for consumption (Michalak et al., 2013).

Water in WLE is typified by high suspended sediment content, meaning it is case 2, optically complex water. As a result, methods used in the open ocean (MODIS, SeaWifs, etc.) do not characterize the blooms extremely well, and often fail in high sediment areas. In addition, blooms may be scum forming at the water surface, violating most open water characterization assumptions. In order to remotely sense these blooms, algae retrieval algorithms need development and testing for a number of hyperspectral sensors.

1.3 Study Area

Lake Erie's Western Basin in the North American Great Lakes is the study area for this research (Fig. 1-1). The Lake Erie Western Basin receives water from discharge from the upper Great Lakes watershed via the Detroit River, the Maumee River, circulation of the Central Basin, and the River Raisin.

Esri, HERE, DeLorme, MapmyIndia, © OpenStreetMap contributors, and the GIS user community

Figure 1-1. Study area of Lake Erie Western Basin.

1.4 Role of Remote Sensing in WLE HABs

Algal blooms of the scale seen in the Western Basin can take some time to develop, sometimes on the order of weeks (Stumpf et al., 2012). Monitoring the development and movement of these blooms has been a priority in aiding our ability to understand and mitigate the harmful effects of the blooms; however our monitoring abilities do not produce the detail needed to do so in timely and cost effective manner. Monitoring of North American HABs is listed as a major research need according to the 2005 International Symposium on Cyanobacterial Harmful Algal Blooms (ISOC-HAB) (Hudnell and Dortch, 2008).

Current bloom prediction practices involve NOAA modeling of total phosphorous load via stream transport into Lake Erie during spring months, which while useful, only provide a general seasonal portrayal of blooms (Stumpf et al., 2012). NOAA also provides bloom intensity maps derived from MODerate resolution Imaging Spectrometer (MODIS) imagery; however the data presented is spatially coarse and is only available on cloud-free days (Stumpf et al. 2012; Wynne et al., 2010). *In situ* measurements of algal concentrations and water constituents involve grab samples of water columns on the lake coupled with detailed analysis of algae taxa and water constituents in the lab. Regular sampling in such a way can provide strong background data to investigate patterns in HAB formation and movement while also providing a basis for comparisons through time and can provide biomass estimates and historical patterns not obtained by other methods (Bridgeman, 2006; Bridgeman et al., 2013). One primary factor derailing progress in HAB monitoring is the sheer size of the study area; it is difficult to collect samples of such a large area of heterogeneous bloom distribution with regularity while the complexity of the system also makes modeling difficult (Chorus and Bartram, 1999).

Satellite and airborne remote sensing can provide sweeping views of the algae problem with regards to the entire basin system (or large parts therein), potentially providing stronger predictive power than discrete, time consuming hand sampling. However, the signal measured at the satellite is not a simple direct measurement of water composition; it represents a composite of interactions in the atmosphere, the water surface, and waterborne components. Atmospheric interference accounts for roughly half of the signal received at the sensor and must be accounted for prior to analysis of water components.

1.5 Optical Properties of Natural Water

Natural water typically includes four primary optical constituents; photosynthetic pigments (mainly chlorophyll), sediment, colored dissolved organic matter (CDOM), and the water itself. Classification of water type is dependent on the relative levels of optical constituents and whether or not they covary. Accurate measurements of remotely sensed information need to take all of these factors into account when examining the electromagnetic radiation (EM) observed by the sensor.

Different remote sensing targets have different optical characteristics. Optical characteristics can depend on the angle of solar irradiance on the object, surface roughness, and even interactions with other objects. An example of this is the appearance of worn down asphalt; while dry it appears light to dark grey but when wet, appears much darker. Another example is while examining a hand specimen of a rock or mineral, it is important to rotate the sample (changing the solar irradiance angle) in order for the angled planes of crystals to glisten and become easier to identify. Optical properties that depend on the medium's chemical makeup and the geometric structure of the radiance distribution are known as apparent optical properties (AOPs) (Mobley, 2010). AOPs are those commonly measured optical properties that give an object its characteristic colors, but are not relatable to concentration in a simple linear relationship.

In addition to AOPs, every object has intrinsic or inherent optical properties (IOPs). IOPs are properties of a medium that do not depend on the geometry of the ambient light field (Mobley, 2010). This means that, in the case of water, the volume has defined scattering and absorption properties regardless of the presence of light (Mobley, 2010). There are three types of IOPs with measureable coefficients; absorption ($\Phi_a(\lambda)$), transmittance ($\Phi_t(\lambda)$), and scattering ($\Phi_s(\lambda)$). Light hitting an object is called incident radiation ($\Phi_i(\lambda)$), which is then absorbed, transmitted, and scattered by the object. Therefore, for a defined volume of water (ΔV) with a defined thickness (Δr), the sum of the light absorbed, transmitted, and scattered will always equal 1, or the amount of incident light originally interacting with the object ($\Phi_i(\lambda) = \Phi_a(\lambda) + \Phi_s(\lambda) + \Phi_t(\lambda)$) (Mobley, 2010).

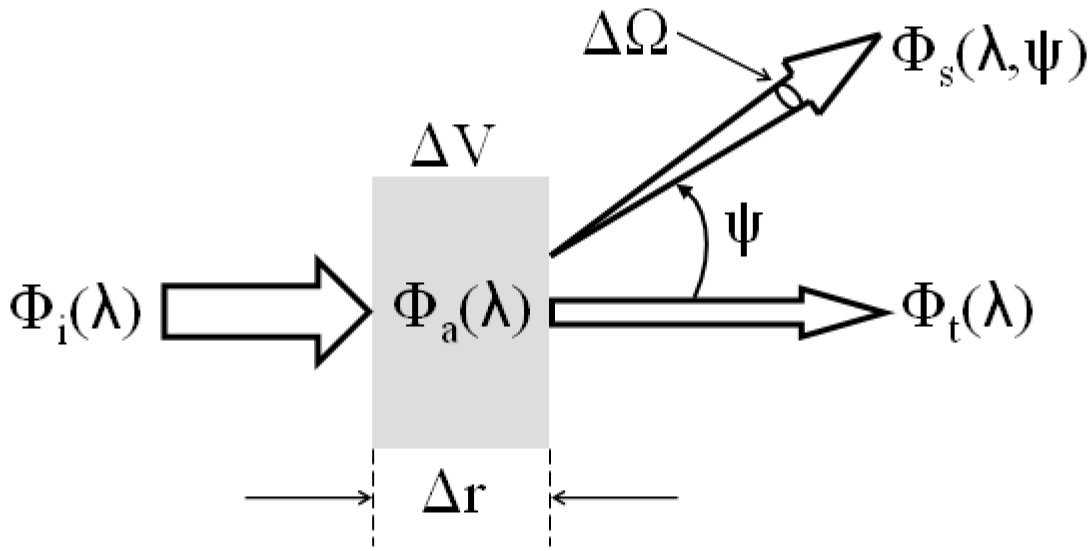

Figure 1-2 Geometry used to define inherent optical properties (Mobley, 2010).

The presence of IOPs gives every target a unique spectral signature, or unique peaks in absorptance and reflectance that are used to identify constituents in water. As IOPs are linearly related to concentrations in water, these become extremely useful in determining water composition. The most common solution to resolving unique spectral signatures is to separate the signals from the media. The spectral signature of Chlorophyll *a* is the most commonly used analogue to algae, and is how the National Oceanic and Atmospheric Administration (NOAA) produces their MODIS cyanobacteria index maps (Wynne et al., 2010). Differentiation of signals is made possible because of *in situ* measurements of water samples that allows for identification of IOPs of water constituents.

1.5.1 Classification of Case 1 and Case 2 Waters

Water bodies are classified by their IOPs in order to simplify measurements and modeling of water optical properties (Sathyendranath, 2000). Classification of water was originally divided into Case 1 and Case 2 by Morel and Prieur (1977) (Morel and Prieur, 1977). Case 1 water color is dominated by phytoplankton while its degradation products, colored dissolved organic matter (CDOM), optically covary with it (Traub, 2012). Case 2 waters are generally nearer to land (coastal) or under the influence of replenishing flow, meaning they are usually shallower. These factors of Case 2 waters mean that CDOM and sediment load have a larger influence on light transfer in the water body (Traub, 2012). As IOPs are linearly related to concentration, i.e. doubling concentration doubles total absorption measured, the increased effect of CDOM and suspended sediments in Case 2 waters makes them inherently optically complex (Traub, 2012). The effects of CDOM and sediment load in Case 2 waters do not covary with chlorophyll levels, meaning that finding the signal of one component cannot be used to mathematically resolve the signal of another (Sathyendranath, 2000).

1.6 Remote Sensing Measurements of Water Bodies

The signal radiating from a water body to a sensor involves more than just light interaction with water and optical constituents through their IOPs but a myriad of other factors as well. Apparent optical properties (AOPs) of the target are dependent on the geometries between the sun, target, and sensor. Reflectance, the AOP that is measured at the surface of the water is related to concentration of water constituents by:

$$R = \frac{Q}{F} * \frac{b}{a+b} \tag{1}$$

$$a = a_{H2O} + a_{doc} + a_{sm} + a_p = a_{H2O} + C_{doc}\sigma_{doc} + C_{sm}\sigma_{sm} + C_p\sigma_p$$

$$b = b_{H2O} + b_{chl} + b_{sm} + b_p$$

Where reflectance equation with R being reflectance, Q reflected radiant flux, F the radiant flux received by the target, b the coefficient of backscattering for each principal optical component of water, and a the coefficient of absorption for each principal optical component of water which is equal to the absorption of water with the concentration (C) and backscattering cross-sectional area (σ) of principal optical components (Bukata et al., 1995).

In addition to AOPs, the atmosphere induces complication due to gaseous absorption and scattering of certain EM wavelengths that either do not reach the sensor or obscure desired signals from the target (Berk et al., 1987). Scattering is problematic in that it sends photons in unpredictable directions as opposed to reflection, which has traceable photon paths (Jensen, 2007). The three types of atmospheric scattering are Rayleigh which scatters in the upper 2 – 8 km of the atmosphere where gas molecules are many times smaller than the wavelength of light passing through them, Mie scattering; also known as aerosol particle scattering, occurs 4.5 km above the Earth's surface where gaseous particles are roughly equal to wavelength, and finally nonselective scattering where gas particles are many times larger than the incoming radiation so all wavelengths are scattered indifferently (Jensen, 2007). Atmospheric variations in temperature, humidity, air pressure, and presence of particulates also play a role in remote sensing complexity, compounding with variance in layers of the atmosphere itself furthers the issue. Rayleigh scattering of the blue EM wavelengths implies that all blue light reaching the water surface is diffuse (Traub, 2012). Cloud cover also has a negative impact on EM reaching a target in many wavelengths.

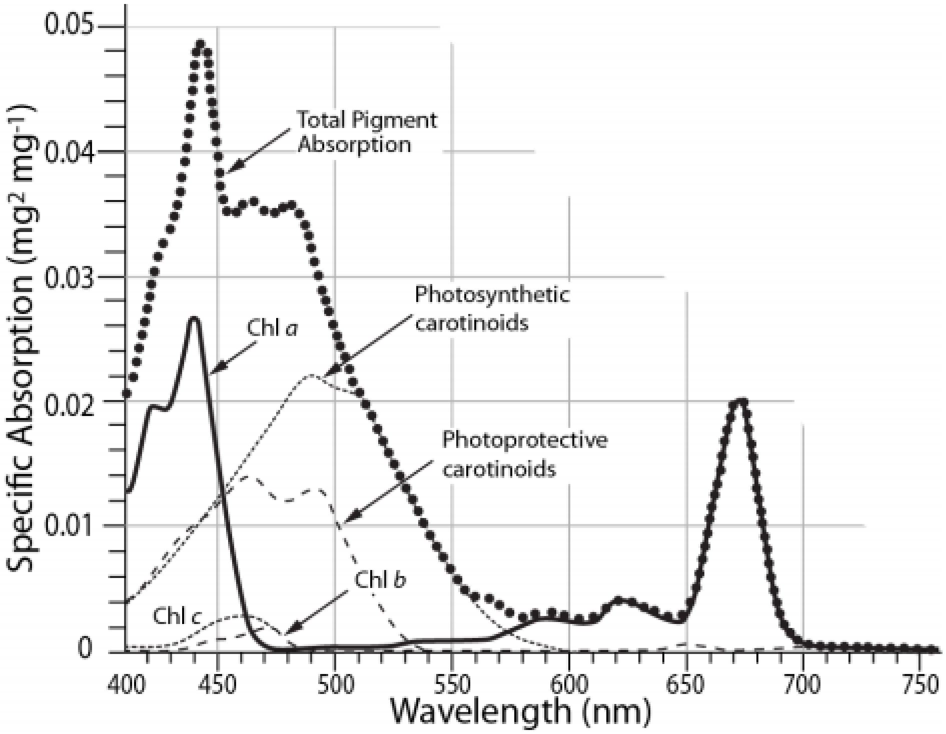

Figure 1-3 Additive Absorption An example of four typical pigments found in oceanic remote sensing. The sum of all four pigments equals the total pigment absorption line. In order to measure one component, the other three must be subtracted. Redrawn from Aiken (1996) by Traub (2012) (Aiken et al., 1996).

Absorption occurs in the atmosphere when radiant energy is absorbed and converted into other forms of energy. Gaseous absorption in the atmosphere is caused by N_2O, O_2, O_3, CO_2, and most importantly in this study, H_2O (Jensen, 2007). H_2O absorption occurs in wavelengths 720, 820, 940, 1100, 1380, 1870, and 2700 nm (Jensen, 2007). H_2O gaseous absorption must be taken into account across these wavelengths as WLE produces immense water vapor via evaporation and that the hyperspectral instruments used cover a broad range of wavelengths.

The air-water interface can act as a reflector to solar irradiance and diffuse radiance (Traub, 2012). Solar geometry, that is, solar zenith angle can cause irradiated light to reflect off of the air-water interface as opposed to passing through it. The presence of wave action, including its respective direction and magnitude also changes solar irradiance geometry, as does surface roughness generated from wind and floating debris.

Electromagnetic radiation leaving the water and air-water boundary must once again pass through the atmosphere before reaching the sensor. Atmospheric interference can scatter light away from the source, and it can also scatter light from outside of the target (off nadir) to the sensor (Kotchenova et al., 2006). In very clear waters, these interactions can mean that the at-sensor signal can be as little as 1% of the original irradiance reaching the surface, however due to the presence of chlorophyll and CDOM in the study area, the actual amount is much greater (Jensen, 2007). Even though objects of interest have known spectral signatures and IOPs, these complications of atmospheric interference, air-water boundary interactions, and solar geometries make target resolution difficult (Bukata et al., 1995).

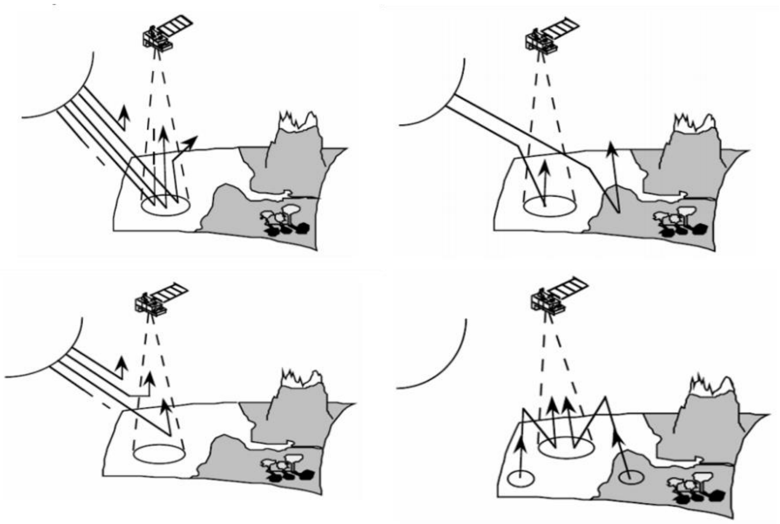

Figure 1-4 Atmospheric Scattering Sketches showing possible radiance paths as affected by atmospheric scattering of off-nadir targets to sensor (Vermote E., 2006).

A look at the general function of subsurface volumetric radiance leaving Case 1 and 2 waters shows how complex the system is:

(2) $$L_v = f[w_{c(\lambda)}, SM_{c(\lambda)}, Chl_{c(\lambda)}, DOM_{c(\lambda)}]$$

where subsurface water leaving radiance (L_v) is a function of the combined concentrations of pure water (w), inorganic suspended materials (SM), organic chlorophyll *a* (Chl), dissolved organic matter (DOM) while accounting for the total absorption and scattering attenuation of each constituent (c(λ)) (Jensen, 2007).

1.7 Remote Sensing of Optical Constituents

1.7.1 Remote Sensing of Chlorophyll

Chlorophyll is present in all photosynthetically active organisms. *Microcystis,* the primary constituent of HABs in western Lake Erie, is a type of plankton called *phytoplankton*, photosynthetic plankton. Jensen (2007) describes plankton as the general term used to describe living organisms, plant or animal, present in a water body that cannot resist the current (Jensen, 2007). Chlorophyll-a in clear water contains four pronounced spectral features in absorption and scattering. Chl *a* absorbs light in the blue region (400 – 500 nm), as well as the red region (~675 nm). Chl *a* has reflectance peaks at 550 nm due to relatively less absorption in the green. It also features a reflectance peak between 690 – 700 nm, caused by algal-cell scattering. The reflectance peak at 690 – 700 nm has been successfully used to measure chlorophyll amount (Rundquist et al., 1995).

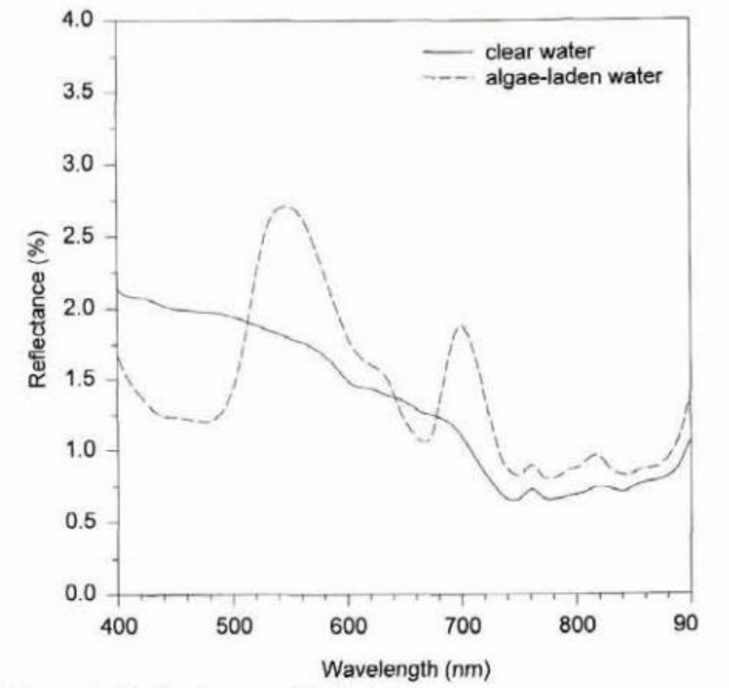

Figure 1-5 Comparison of reflectance spectra of clear water and algae-laden water (Han, 1997).

1.7.2 Band Ratios for Chlorophyll Estimates

As a result of these absorption peaks, in case 1 clear water, there is a strong correlation of chlorophyll *a* and water leaving radiance (L_{w}). The general equation

$$R_{\lambda 1,\lambda 2} = \frac{L_w(\lambda_1)}{L_w(\lambda_2)} \qquad (3)$$

shows how a ratio of radiances yields reflectance, where R is reflectance of the ratio of water leaving radiance at two bands (x and y). Radiances however do not directly relate to concentration of water constituents; however a ratio of radiances can be related to concentration, by utilizing eq. 1 for two wavelengths of interest to generate the ratio. Wavelengths typically used in a chlorophyll *a* ratio are ~670 nm and ~427 nm. Chlorophyll *a* has absorption peaks at these wavelengths, so a ratio between them reveals where reflectance peaks and thus makes the presence of Chlorophyll *a* identifiable.

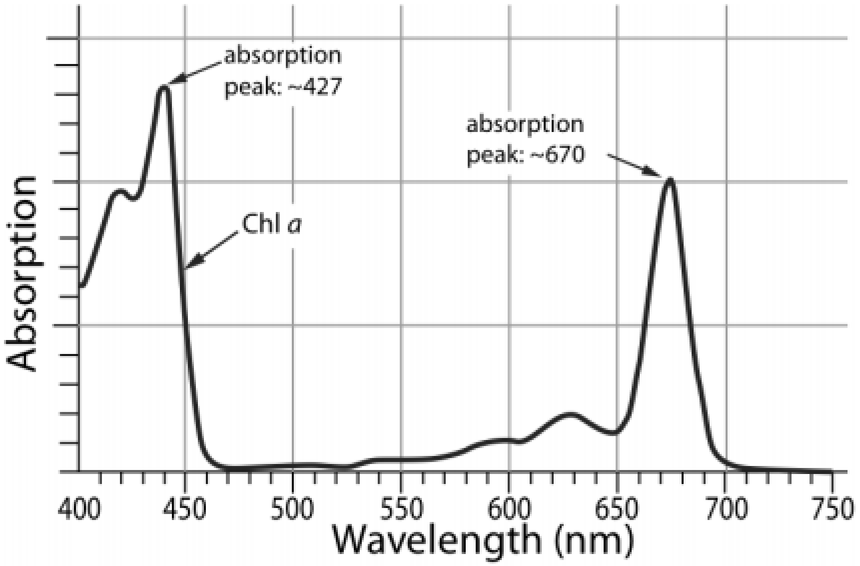

Figure 1-6 Absorption curve of chlorophyll *a* where pigments have low absorption, they will have high reflectance (Traub, 2012).

1.7.3 Suspended Sediment and Minerals

Particles suspended in the water column can range in size from fine clay (3 – 4 µm) to coarse grained sand (131 – 250 µm). Input of these minerals into western Lake Erie comes largely from agricultural runoff in the Maumee River watershed. Measured spectral reflectance of the sediment depends on the particle size and type (IOPs of each type) as well as overall abundance of sediment. In order to differentiate the remote sensing signal of suspended sediment, *in situ* observations must be made and then compared to signals from the sensor. For turbid waters, Binding et al. (2005) found that NIR wavelengths are suitable to study suspended sediments due to the fact that suspended sediment can allow sufficient scattering to overcome the NIR absorption of water. In less turbid waters, successful correlation between suspended sediment and visible EM was found by Miller and McKee (2004) with MODIS band 1 (620- 670 nm) and again by Binding et al. (2005) at 665 nm (Jensen, 2007).

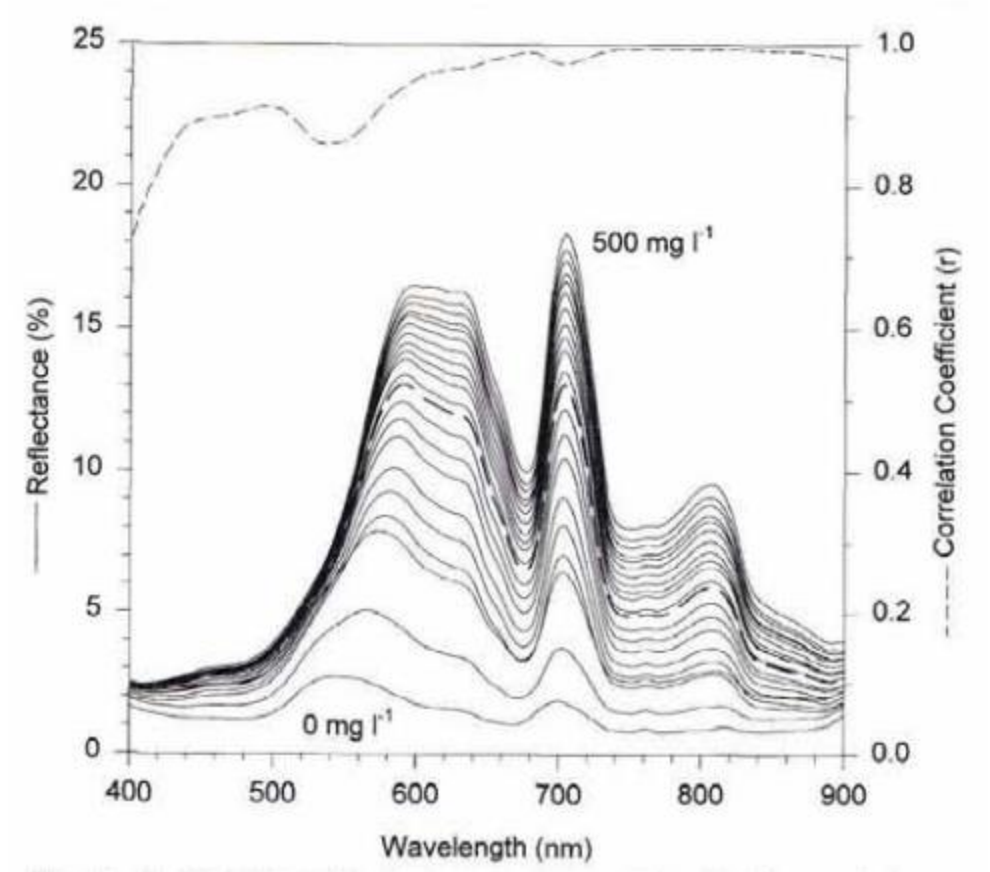

Figure 1-7 Suspended sediment reflectance comparison of percent reflectance of algae-laden water with varying concentration of suspended sediments ranging from 0 – 500 mg/l (Han and Rundquist, 1997).

1.7.4 Colored Dissolved Organic Material

Phytoplankton living in the photic zone (vertical portion of the water surface to the 1 percent subsurface irradiance level) produces organic matter via photosynthesis (Jensen, 2007). Colored dissolved organic material (CDOM) is also generated in the photic zone from zooplankton consuming the phytoplankton, generating CDOM as a byproduct, and from bacterioplankton decomposing organic matter generated from phyto- and zooplankton. In some cases, CDOM can diminish the penetration of light in the water column (Bukata et al., 1995). Decomposition of these plankton cells yields carbon dioxide, inorganic nitrogen, sulfur, and phosphorous compounds (Jensen, 2007). Additionally, humic substances can be produced which are sometimes called Gelbstoffe or yellow substances which can change the overall color of the water in addition to changing absorption and scattering IOPs (Jensen, 2007).

CDOMs can make remote sensing of chlorophyll even more of a challenge. CDOMs strongly absorb EM in the UV and blue wavelengths. Chlorophyll *a* and CDOM share some overlap in absorption features, making direct analysis of chlorophyll *a* difficult. This is especially true because CDOM and chlorophyll *a* have the same absorption coefficient at 440 nm in oligotrophic ocean (Carder et al., 1989).

1.7.5 Remote Sensing of Chlorophyll *a* in Lake Erie

The most common method of studying algae by remote sensing is to relate algae-dominated chlorophyll reflectance peaks to *in situ* measurements of the algae. Generally, algae possess a handful of various pigments (multiple types of chlorophyll, Phycocyanin, phycoerythrin, etc.), however chlorophyll *a* is common to all aquatic algae species. Simple measurements of green spectrum reflectance are not suitable for algae identification as general green reflectance is not unique to algae. Chlorophyll *a* is unique to photosynthetic organisms and has IOPs that result in absorbance peaks at 420 nm and 670 nm, which is useful in identifying terrestrial plant life. For aquatic algae, however, water absorbs EM in the 670 nm wavelength which makes aquatic algae identification more complex than a simple band ratio.

NOAA produces cyanobacteria index (CI) maps to provide a general understanding of algae blooms in Western Lake Erie. NOAA produces these maps, which show concentration of chlorophyll *a*, by analyzing the spectral curvature between three MERIS bands (8, 7, and 9 at 681 nm, 709 nm, and 665 nm respectively). Three bands, as opposed to two in a band ratio, measures the spectral shape (or curvature) of 681 nm while allowing for less than ideal atmospheric correction (Wynne et al., 2010). Curvature around 681 nm was chosen because scattering effects of cyanobacteria have found to peak near 700 nm, so the strength of the curvature can show concentration of cyanobacteria (Gitelson, 1992; Wynne et al., 2010). Wynne et al. (2010) used the following equation

$$CI = -SS(681) \tag{4}$$

where cyanobacteria index (CI) is equal to the negative spectral shape (SS) at 681 nm where

$$SS(\lambda) = R(\lambda) - R(\lambda^{-}) - \{R(\lambda^{+}) - R(\lambda^{-})\} \times \{(\lambda - \lambda^{-}) \div (\lambda^{+} - \lambda^{-})\} \tag{5}$$

and R = reflectance, λ = 681 nm (MERIS band 8), λ^{+} = 709 nm (band 9), λ^{-} = 665 nm (band 7) (Wynne et al., 2010). In this way, spectral shape results in the second derivative which makes the equation insensitive to poor atmospheric correction (negative radiances) unlike band ratios which can be ruined by negative radiances (Wynne et al., 2010).

Another well-supported technique for monitoring HABs in the North American Great Lakes Region is the Color Producing Agent Algorithm (CPA-A) produced by Michigan Tech Research Institute (MTRI). By utilizing measured concentrations of color producing agents (Chlorophyll-a, dissolved organics, and suspended minerals) along with backscattering and absorption coefficients with each (derived from a hydro-optical (HO) model), CPA-A can successfully be used to relate Chl-a levels to HAB events (Shuchman et al., 2013).

The CPA-A equation is as follows:

(6) $$Rrs_i = -0.00036 + 0.110\left(\frac{b_i}{a_i}\right) - 0.0447\left(\frac{b_i}{a_i}\right)^2$$

$$a_i = a_{H2O,i} + C_{chl}a_{chl,i} + C_{doc,i}\,a_{doc,i} + C_{sm}a_{sm,i}$$

$$b_i = b_{H2O,i} + C_{chl}b_{chl,i} + C_{sm}b_{sm,i}$$

Where,

C	Vector representing concentrations of each CPA
a_i	Bulk absorption coefficient for each CPA at band *i*
b_i	Bulk backscattering coefficient for each CPA at band *i*

The CPA-A method relies on excellent atmospheric correction and does not directly produce cyanobacteria results like the CI method. CPA-A was made specifically for the Great Lakes, like the CI algorithm, however the coefficients used in the equation are generated from HO models specific to each lake, generating adequate Chl-a concentrations, while also being applicable to a range of sensors (Shuchman et al., 2013).

1.7.6 Optical Constituent Sources for WLE

Western Lake Erie receives input from multiple watersheds, each with varying soil and geology types, and influenced by varying degrees of agricultural applications and urban development. The largest source of water is from the upper Great Lakes watershed, fed to Lake Erie by way of the Detroit River. The next largest, and the largest source of sediment into Lake Erie, is the Maumee River watershed which extends into Indiana and southern Michigan. The rest of the large tributaries include the River Raisin of Monroe, Michigan, the Sandusky River flowing into Sandusky Bay and then into Lake

Erie, and the Huron River which passes its water through marshes in Monroe and Wayne counties of Michigan and then to Lake Erie.

The dominant optical component of Western Basin waters is suspended mineral sediment. Though the draining of the upper Great Lakes watershed brings about 90% of water input to Western Lake Erie, it provides very little sediment load. Conversely, the Maumee and Sandusky watersheds lie in an old glacial lake plain, formed when glaciers retreated from the area about 11,000 years ago leaving behind fine-grained sediments. These fine-grained sediments provide fertile soils used extensively in agriculture, but are also prone to erosion. Clay sized sediments as small as 3 – 4 µm are easily eroded from farm fields and are carried into western Lake Erie by the Maumee and Sandusky Rivers, where the particles remain in suspension and have levels of backscattering (Brady and Weil, 2008).

Seasonality causes tributary flow to fluctuate greatly over time, creating different CDOM and algal characteristics throughout the year. Windy conditions on Lake Erie can cause sediment re-suspension which can also change the color of the water. Spring months bring thawing and liquid precipitation to the Maumee watershed which flushes the agricultural top soil into the River. This spring flush differs from summer erosion as the temperature difference mean the organic materials have not gone through a complete chemical decomposition as opposed to sediments transported in the summer months (Benner and Kaiser, 2011). Algae populations can vary in biochemical makeup as seasonality progresses, even after death their decompositions change in rates and products of humic and fulvic acids as summer progresses. Limestone bedrock underlies

Western Lake Erie and maintains a slightly alkaline pH level which can increase rates of humic and fulvic acid decomposition (Hargreaves, 2003; Reche et al., 1999).

1.7.7 Historical Development of Aquatic Remote Sensors

Early research in oceanic optical properties got its start in the 1950s when investigations were being made into submarine warfare (Preisendorfer, 1976). In the early 1960s the Environmental Research Institute of Michigan (ERIM) held the first technical conference of remote sensing in the United States and possibly the world, and was sponsored by the U.S. Navy's Office of Naval Research in 1962. It was not until ten years later, in 1972, that the Multispectral Sensor (MSS) was made a part of Landsat 1 which allowed satellites to expand their usage from meteorological data to applications of optical remote sensing (NASA, 2016). The first MSS was not designed for aquatic remote sensing but it did pave the way for the Multispectral Scanner System to be utilized by Landsat 4 and future missions (NASA, 2016).

Since the beginning, satellite remote sensing was held back due to technological restrictions, cost, and size limits which meant that early sensors had broad spectral bandwidth and low radiometric resolution. Only a small amount of bandwidth data could be transmitted to terrestrial receivers, meaning that each field-of-view (FOV) pixel only offered coarse information (Jensen, 2007). The first Landsat MSS only had four bands that monitored the EM spectrum, 0.5 to 0.6 µm (Green, band 4), 0.7 to 0.8 µm (red, band 5), 0.8 to 0.9 µm (reflective near-infrared, band 6), 0.9 to 1.0 µm (reflective near-infrared, band 7) (Jensen, 2007). The bandwidths had to be so coarse in order to maintain a usable signal-to-noise ratio without sacrificing spatial resolution (Jensen, 2007). The omission of a blue band hindered the ability of the first Landsat to be used as an aquatic sensor, and was not included due to the inability at the time to eliminate atmospheric interference at that wavelength.

Aquatic remote sensing hit its stride in 1999 with the launch of the Moderate Resolution Imaging Spectroradiometer (MODIS) mission. MODIS features nine bands that are specifically geared for aquatic remote sensing (bands 8 – 16) featuring wavelengths of .405 - .877 μm in 10 μm bandwidths (Jensen, 2007). This finer bandwidth allows MODIS to differentiate signals that activate its sensors, as opposed to Landsat which was largely impossible to pinpoint different sources at one broad bandwidth (sources of water coloration, for example) (Figure 1 – 8).

The precision of MODIS was surpassed by the European Space Agency's Envisat and its Medium Resolution Imaging Spectrometer (MERIS). While MERIS features the same spectral bandwidth of MODIS, it features spatial resolution of 300 m square as opposed to the 1,000 m square of MODIS. This increase in spatial resolution meant that coastal waters, and thereby lakes, could be remotely sensed as opposed to open ocean and land being the main focus of remote sensing.

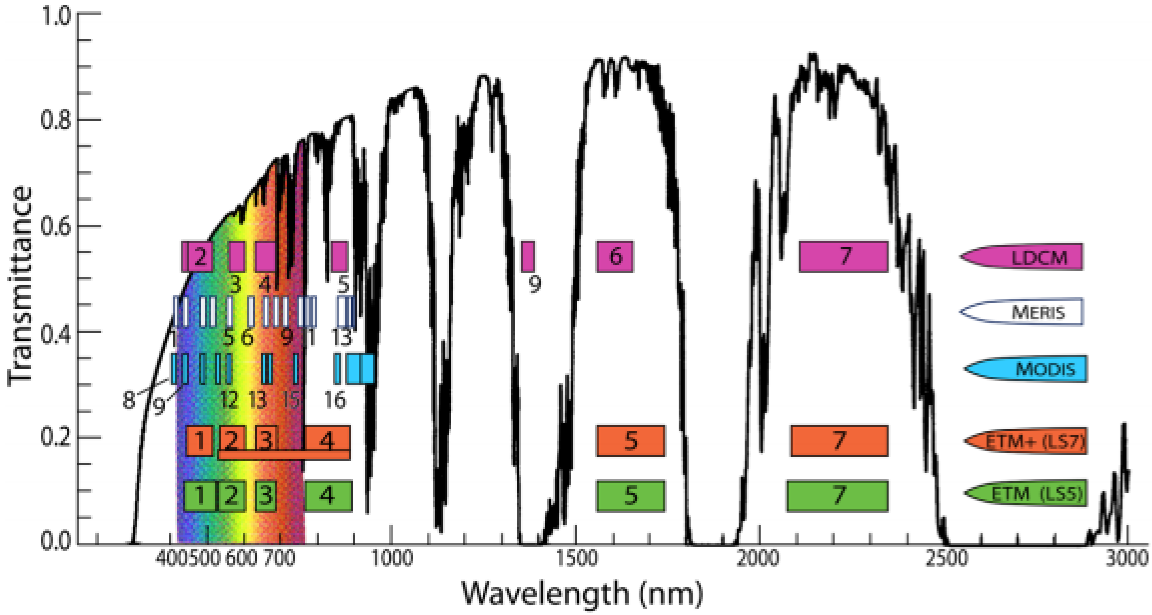

Figure 1-8 Comparison of Sensor Bands Various sensors arranged by age (oldest on bottom). The width of the band rectangle indicates spectral bandwidth per band number. Band numbers assigned by instrument designers. Transmittance spectrum after Berk (Berk et al., 1987). Figure by Traub (Traub, 2012).

1.7.8 Hyperspectral Sensors Used in this Study

Modern multispectral imagers such as MERIS and MODIS provide the ability to remotely sense aquatic targets, but they do still leave a lot to be desired. Hyperspectral imagers typically acquire data on the order of hundreds of spectral bands as opposed to tens of bands or even less (Jensen, 2007). The narrow bandwidths and broad spectrum coverage provided by hyperspectral imagers allow for maximization of contrast between the target signal and background noise (Jensen, 2007).

NASA's Hyperspectral Imager for the Coastal Ocean (HICO) is a hyperspectral imager onboard the International Space Station (ISS). It features a roughly 90 m square spatial resolution, featuring 128 bands with a spectral resolution of 5.7 nm making it ideal for coastal water applications (Lucke et al., 2011). HICO was operational from September 25, 2009 – September 13, 2014 (Lucke et al., 2011).

NASA Glenn Research Center (NASA GRC) designed an airborne hyperspectral imager (HSI) that is used in studying Lake Erie. Originally developed in 2006 and updated in 07 – 08, the GRC's HSI features a 16° FOV (resulting in ~10m resolution at study altitudes) with a spectral range of 400 – 900 nm (2.5 nm bandwidth). The GRC HSI allows for lake observations to be made below the cloud deck on cloudy days which would render a satellite sensor useless.

Hyperspectral measurements taken on the lake were done so using an ASD FieldSpec 3 Hi Res Spectroradiometer (ASD). The instrument features a spectral range of 300 – 2500 nm at 2 nm bandwidths.

1.7.9 Implications of Hyperspectral and Airborne Sensors

Multispectral instruments that are typically used have bandwidths that are specifically chosen to align with atmospheric windows to allow for ease of atmospheric corrections. Hyperspectral imagers, however, measure continuously across the electromagnetic spectrum regardless of atmospheric window presence, so robust atmospheric correction is necessary for hyperspectral instruments to be used effectively.

The airborne HSI used in this investigation offers an advantage over satellite sensors with its ability to fly below the cloud deck, allowing for data collection on days where MODIS would have delivered a "no data" scene. Flying below cloud deck, however, results in less spatial coverage of the blooms compared to satellite, but the ability to negate cloud coverage while also providing hyperspectral data proves to be more useful than the minor hindrance of small spatial coverage.

1.8 Hypothesis

It is accepted that current algae retrieval algorithms based on multispectral sensors used in Case 1 waters do not provide adequate algae mapping products in Western Lake Erie's Case 2 waters. This project is meant to improve methods leading to HABs mapping by testing different algal retrieval algorithms and atmospheric correction techniques using a three tiered hyperspectral sensor approach utilizing satellite (HICO), airborne (HSI), and ground level sensors (ASD), coupled with water quality measurements as reference data (cyanobacteria concentration, turbidity, and total suspended solids).

Chapter 2

Methods

2.1 General Methods

As stated briefly in chapter 1, the object of this investigation is to test algae retrieval algorithms and atmospheric correction techniques using satellite, airborne, and ground based hyperspectral instruments in order to improve methods leading to HABs mapping.

Water based testing involved taking water samples and spectrometer readings at several sample sites in the Western Basin. Water sampling produced measured concentrations of cyanobacteria, total suspended solids, turbidity, photosynthetically active radiation, and other parameters were recorded for each sample.

Airborne spectrometer data was flown on the same day, or nearly the same day, as on-lake expeditions, when weather allowed. Airborne measurements were atmospherically corrected via the vicarious method. Corrected images were processed using the Wynne CI (Wynne et al., 2010) and then compared against measured cyanobacteria concentrations. A flowchart of these processes is illustrated in figure 2-1. Sample measurements were compared with airborne and satellite measurements to determine accuracy of different methods of atmospheric correction and algorithm application.

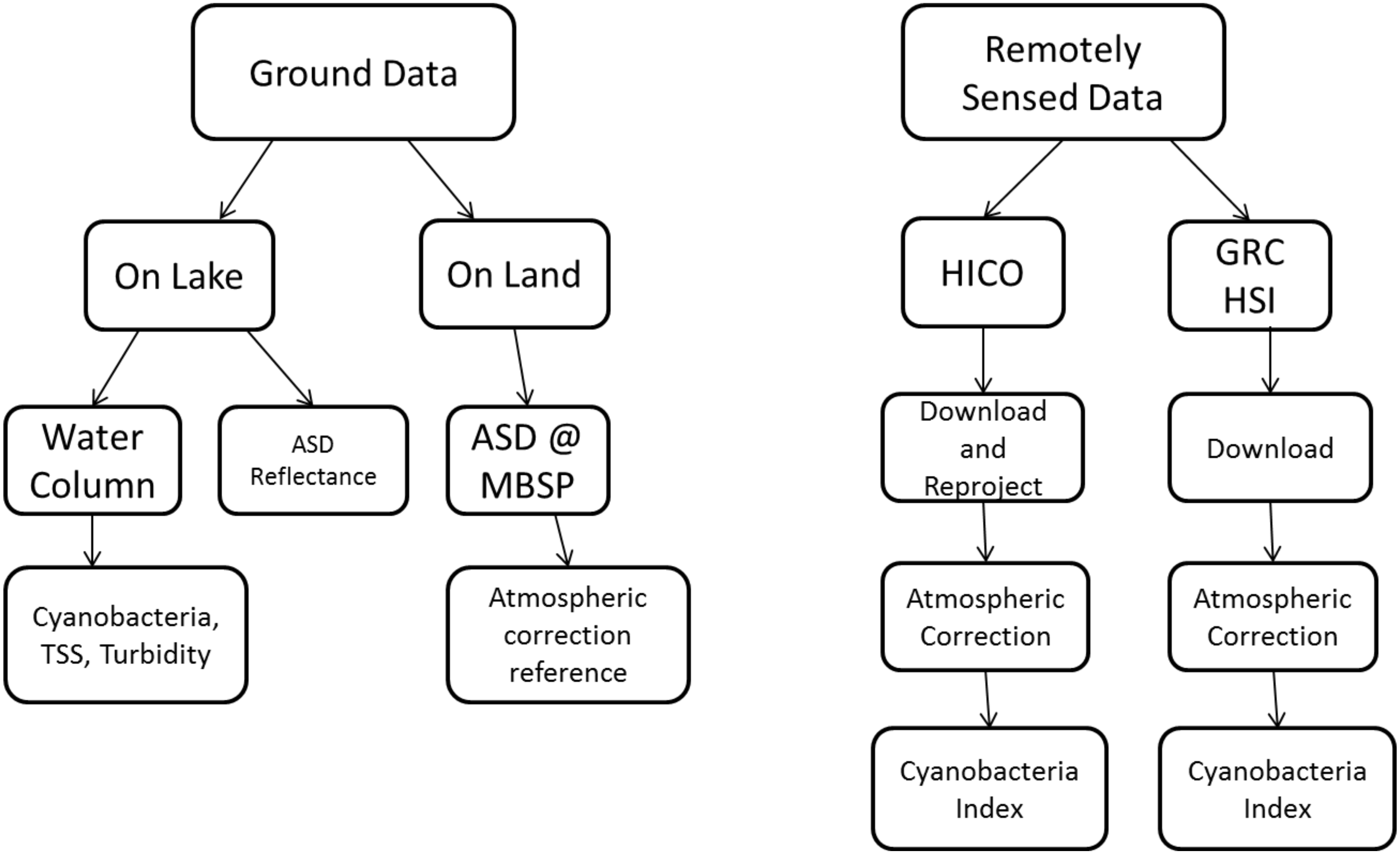

Figure 2-1 Flowchart showing the general methods used in this investigation for data collection and product creation.

2.2 Sampling

On-lake spectrometer readings and water samples were collected at various sampling points in Lake Erie's Western Basin. Two sampling circuits were alternated; the "Standard" circuit of the Toledo water intake (Crib), and points GR1, 4P, MB18, MB20, 7M, and 8M and the "Erie West" points of EW1 – EW5 (Figure 2-2). The sampling points were chosen in order to collect samples from both near-shore and mid-lake locations while also covering a broad area of Western Lake Erie. These sampling points are the same points used by Dr. Thomas Bridgeman at the University of Toledo Lake Erie Center Western Lake Erie Limnology Laboratory (WLELL) for their long standing studies and allows for comparison of future and past lake investigations. On-lake spectrometer and total suspended solids (TSS) measurements were piggybacked onto WLELL's cruises which allows for the data to be taken in respect to other environmental parameters.

2.2.1 Sample Locations

The Standard Circuit includes seven sampling sites. Two of which are located in Maumee Bay (MB18, MB20), two are open water sites (8M, 7M), one is in the dredged shipping channel (GR1), one is near the northern shore of West Sister Island (4P) and one point at the Toledo water intake (Crib). The Erie West circuit features five sampling sites. Of these points, two of them overlap the Standard circuit; EW1 being the Crib and EW3 being 7M. The other three points are near-shore with EW5 corresponding to the location of the WLELL Buoy. The boat is anchored at the latitude and longitude of the locations to prevent drift once on-site.

Figure 2-2 Study area of Lake Erie's Western Basin. Dots indicate *in situ* hyperspectral and water measurements.

2.2.2 Sampling Methods

Water samples were collected through the water column using a PVC pipe of varying lengths based on depth of water at each site (2 m at MB18, MB20, 5 m at 7M, CRIB, and 8M, and 9 m at 4P and GR1). Water collected was stored in 1 L opaque HDPE bottles. Prior to lake excursions, the bottles were washed in RO water with a non-phosphate liquid soap, immersed in a dilute HCl acid bath, rinsed twice in RO water, and set to dry. During lake operations, the water column was sampled by the PVC sampling tube and deposited into a bucket that had been rinsed with lake water from the surface at that location. Water in the bucket was then stirred to allow an even distribution of suspended materials and then transferred to two 1 L bottles, which had also been rinsed with lake water from the sampling site. Filled bottles were transferred to an ice filled cooler to retard decay and biological processes. Location, date, and time were collected for each bottle, written on tape. Environmental data were also recorded including water temperature, wind speed and direction, wave height, cloud cover, and Secchi depth. Dates of water sampling collection are shown in table 2.1 and 2.2.

Table 2.1 TSS, Cyanobacteria, and Turbidity measurements with coincident ASD data of 2014

Date	Site	TSS (mg/l)	Cyanobacteria (µg/l)	Turbidity
7/24/2014	CRIB	16.92308	9.58971	*
7/24/2014	4P	4.1666667	5.38278	*
7/24/2014	GR1	3.5294118	8.54451	*
7/24/2014	8M	7.8181818	19.5975	*
7/24/2014	MB18	16	50.9535	*
7/24/2014	MB20	22.333333	34.4916	*
7/24/2014	7M	9.8823529	10.73943	*
8/6/2014	CRIB	*	50.6922	*
8/6/2014	4P	7.0833333	20.56431	*
8/6/2014	7L		12.2811	*
8/6/2014	GR1	4.3076923	4.05015	*
8/6/2014	8M	16.666667	23.88282	*
8/6/2014	MB18	32.5	34.88355	*
8/6/2014	MB20	20	109.746	*
8/6/2014	7M	13.529412	61.4055	*
8/14/2014	GR1	5.8715847	6.76767	0.885714
8/14/2014	4P	8.3590909	12.25497	6.371429
8/14/2014	8M	9.9107143	19.5104	11.66667
8/14/2014	7M	39.333333	50.6051	37.6
8/14/2014	CRIB	33.076923	55.591575	45.38
8/14/2014	MB18	32.1875	74.7318	41.83333
8/14/2014	MB20	20.969231	60.6216	22.73333
8/27/2014	GR1	3.9582346	5.93151	0.166667
8/27/2014	4P	7.8181818	16.43577	3.422222
8/27/2014	8M	25.5	28.743	22.4
8/27/2014	7M	27.285714	32.97606	24.2
8/27/2014	CRIB	31.75	15.20766	35.4625
8/27/2014	MB18	35.705128	64.69788	32.9
8/27/2014	MB20	45.5	45.77976	31.75
9/14/2014	GR1	33.904762	7.91739	2.355556
9/14/2014	4P	11.166667	6.7938	3.785714
9/14/2014	8M	20.5	19.4233	19.85714
9/14/2014	7M	10.833333	7.1422	6.116667
9/14/2014	CRIB	18	18.50875	17.41429
9/14/2014	MB18	11.217949	18.50875	11.475
9/14/2014	MB20	12.461538	13.065	11.66667

All dates are 2014. Asterisks indicate missing data

Table 2.2 TSS, Cyanobacteria, and Turbidity Measurements with coincident ASD data of 2015

Date	Site	TSS (mg/l)	Cyanobacteria (µg/l)	Turbidity	Date	Site	TSS (mg/l)	Cyanobacteria (µg/l)	Turbidity
6/5/2015	GR1	4.943182	0.5	*	8/4/2015	EW1	12.625	*	*
6/5/2015	4P	10.1	1.4	*	8/4/2015	EW3	9.545455	*	*
6/5/2015	8M	29.8	3	*	8/4/2015	EW5	10.5	*	*
6/5/2015	7M	18.5	3.1	*	8/10/2015	GR1	7.17938	9.7	3.93
6/5/2015	MB18	26.65789	3.1	*	8/10/2015	4P	8.198198	38.6	7.99
6/5/2015	MB20	40.61905	6.9	*	8/10/2015	8M	37.51361	162.4	14.38
6/5/2015	CRIB	19.52564	1.7	21.86	8/10/2015	7M	17.95635	55.1	6.31
6/16/2015	GR1	3.073684	0.3	1.8	8/10/2015	MB18	15.94783	31.8	17.13
6/16/2015	4P	2.081389	0.8	0.91	8/10/2015	MB20	23	25.5	29.25
6/16/2015	8M	7.176471	0.9	6.84	8/10/2015	CRIB	30.36765	50.4	6.3
6/16/2015	MB18	9.428571	1.4	8.09	8/17/2015	EW1	13.55385	*	*
6/16/2015	7M	5.253061	0.8	4.59	8/17/2015	EW2	13.66957	*	*
6/16/2015	MB20	80.5	3.7	108.14	8/17/2015	EW3	13.15705	*	*
6/16/2015	Crib	8.649828	0.8	8.17	8/17/2015	EW4	15.12308	*	*
7/1/2015	Crib	31.81818	1.5	43.93	8/17/2015	EW5	22.66667	*	*
7/1/2015	GR1	7.714286	1.2	7.44	8/28/2015	8M	14.51042	26.8	13
7/1/2015	4P	22.2	1.6	26.63	8/28/2015	7M	11.27027		10.47
7/1/2015	8M	11.18182	1.3	19.19	8/28/2015	Crib	11.43581	36.4	28.53
7/1/2015	7M	28	1.8	38.8	8/28/2015	MB18	14.66667	1.4	49.8
7/1/2015	MB18	55.38636	2.1	14.65	8/28/2015	MB20	16.33333		18.31
7/1/2015	MB20	41.75	2	47.21	8/28/2015	Buoy	16.85185	*	*
7/20/2015	EW5	15.71429	1.9	*	9/8/2015	7M	10.80952	9.4	6.18
7/20/2015	EW1	10.59722	2.8	*	9/8/2015	8M	8.2	0.4	1.63
7/20/2015	EW3	7.363636	1.3	*	9/8/2015	Crib	17.53333	15.7	8.48
7/27/2015	GR1	1.978296	*	0.58	9/8/2015	EW5	11.09375	10.9	8.79
7/27/2015	4P	1.226721	*	0.77	9/8/2015	MB18	15.83333	16.5	11.14
7/27/2015	8M	3.3	*	4.64	9/8/2015	MB20	20.8	20	10.9
7/27/2015	7M	9.666667	*	3.29	9/15/2015	4P	23.63636	25.3	14.15
7/27/2015	MB18	19.53333	*	15.32	9/15/2015	GR1	*	8.9075	*
7/27/2015	MB20	24.75	*	25.94	9/15/2015	8M	*	19.45667	*
7/27/2015	CRIB	6.777778	*	3.33	9/15/2015	7M	*	12.842	*
8/4/2015	EW1	12.625	*	*	9/15/2015	Crib	*	28.18091	*
8/4/2015	EW3	9.545455	*	*	9/15/2015	MB18	*	23.225	*
8/4/2015	EW5	10.5	*	*	9/15/2015	MB20	*	21.73813	*

All dates are 2015. Asterisks indicate missing data

2.2.3 Transporting and Storing Samples

Once on-lake excursions were complete, samples were transported back to the lab in a cooler on ice. Samples that were not immediately processed were stored in a cooler at WLELL at 6 °C.

2.3 Measuring Physical Properties

Immediately following a sampling trip, samples were tested for total suspended solids (TSS), chlorophyll and phycocyanin concentration, and turbidity.

2.3.1 Preparing for TSS and Chlorophyll measurements

Filtering was done using 47 mm diameter Whatman GF/F filters with a pore size of 0.7 μm. Filters were stored in aluminum pouches fitted to hold individual filters and were numbered with a stylus in order for the label to withstand high temperatures.

Filters needed to be prepared before analysis began. First, filters were rinsed with 60 ml of RO water. Filters were then dried in a muffle furnace for 15 minutes at 550 °C. Filters were again rinsed in 60 ml of RO water, and dried again for one hour in an oven at 97 °C to 103 °C. Filters were transferred immediately from the furnace storage to a desiccator to prevent weight gain from atmospheric absorption. Weighing began as soon as possible after the final heating. Filters were weighed to the nearest 0.1 mg, the scale used depended on available lab space at the time of weighing.

Devices used for TSS processing include 500 ml vacuum flasks and Gelman Sciences 47 mm magnetic filter funnels, which were cleaned in the same manner as the HDPE bottles in Section 2.2.2.

Two filter replicates were measured per sample location, per trip.

2.3.2 TSS Measurement

Sampled water was run through the prepared filters via motorized vacuum pump. The amount of water pumped through a filter was dependent on how quickly the water drained. Once water appeared to stagnate, no further water was added, and the amount ran through the filter was recorded. The second 1 L bottle was used on the second filter, regardless of amount of water used on the first filter, producing a duplicate of each sample site. Vacuum was kept below 80 mm Hg in order to avoid rupturing of plankton cells, which would cause the chemical makeup of the filtered sample to be different from the water sample. Used filters were dried in an oven between 97 °C to 103 °C, depending on the oven used, for one hour. Dried filters were weighed, and reinserted into the oven for 15 additional minutes and weighed again to ensure the weight had stabilized. Once dried weight had stabilized, the original filter weight was subtracted from the newly dried weight to produce the weight of TSS.

2.3.3 Chlorophyll *a* Measurement

Dr. Tom Bridgeman's lab at the WLELL provided chlorophyll *a* concentrations. Chlorophyll was extracted from water samples run through a BBE FluoroProbe lab station. A detailed explanation to Dr. Bridgeman's methods can be found in Bridgeman, Chaffin, Filbrun 2013 (Bridgeman et al., 2013).

2.3.4 Phycocyanin Measurement

Dr. Tom Bridgeman's lab at the WLELL provided Phycocyanin concentrations. Phycocyanin was extracted from water samples run through a BBE FlouroProbe lab station.

2.3.5 Turbidity Measurement

Turbidity is the measurement of water clarity. Turbidity is measured by a YSI sonde, calibrated with turbidity standards, dropped through the water column and measured continuously throughout at each of the sample points. Turbidity is expressed in nephelometric turbidity units (NTUs).

2.4 Spectral Data Collection

Dates of hyperspectral data collection for ASD, HSI, and HICO are shown in tables 2.3-5.

2.4.1 Ground Level Spectrometer Measurements

An ASD FieldSpec 3 Hi Res Spectroradiometer (ASD) was used to measure reflectance from the water's surface. At the wavelengths of interest, 400 to 900 nm, the ASD has a spectral resolution of 1 nm.

While on the lake, once anchored to the sampling location, the boat was allowed to stabilize its direction. Once stable, the ASD and calibrated Labsphere spectralon plate were brought to the portion of the boat illuminated by the sun, to avoid shadowing. The ASD was then calibrated against the spectralon plate by using the "white reference" tool in the ASD software. The ASD was then taken in hand and leaned over the side of the boat, taking care to avoid the boats reflection in the water, and a reflectance measurement was taken. Each ASD measurement consisted of 50 samples, taken 4 times, adding to an average reflectance derived from 200 readings. A duplicate measurement was performed by again calibrating and measuring over the water.

On the ground, ASD measurements were taken at Maumee Bay State Park's parking lot following the same procedure as on the lake. These measurements were used as dark references in order to atmospherically correct remotely sensed images using the empirical line method as described in section 2.5.1.

Great care was taken to avoid changes in solar illumination. If by chance a change in cloud cover occurred while calibrating or measuring, that measurement was marked as a bad sample and the calibration step began again once the sunlight stabilized.

2.4.2 ViewSpec Processing of ASD Spectral Measurements

Reflectance measurements taken by the ASD are saved as *.asd.txt* files and were processed to show reflectance values in ViewSpec Pro, Ver. 5.6, software (ASD Inc., Boulder, CO).

2.4.3 Airborne Spectrometer Measurements

NASA Glenn Research Center (GRC) of Cleveland, OH operated an airborne hyperspectral instrument (HSI). In the summer of 2014, the HSI was flown on an S3 jet and in 2015 was flown on a Twin Otter. The HSI is a push broom sensor with a very high signal to noise ratio (> 800). It features a field of view (FOV) of 16° and is flown to an average altitude of 3,000 ft in 2015 and between 3,000 and 10,000 ft for 2014. The HSI has a spectral range of 400 – 900 nm, with a spectral resolution of 2.5 nm. GRC HSI data was distributed by GRC via Ohio Super Computer. Processing for geometric and radiometric corrections was performed by Bob Anderson of NASA GRC.

2.4.4 NASA HICO Data

NASA’s Hyperspectral Imager for the Coastal Ocean (HICO) is a hyperspectral imager onboard the International Space Station (ISS). It features a roughly 90 m square spatial resolution, 128 bands with a spectral resolution of 5.7 nm making it ideal for coastal water applications (Lucke et al., 2011). HICO was operational from September 25, 2009 – September 13, 2014 (Lucke et al., 2011).

Unfortunately, HICO became unresponsive in 2014, so any discussions of HICO throughout only refer to the field work of 2014.

2.5 Atmospheric Correction of Remotely Sensed Data

One goal of this project was to test and compare different atmospheric correction techniques. One method utilized the 6Sv code to atmospherically correct images in an automated matter. 6Sv, Second Simulation of a Satellite Signal in the Solar Spectrum, is the vector based version of an RT code that utilizes the MODIS based look-up tables for atmospheric corrections (Vermote E., 2006). 6Sv allows for the simulation of space- and airborne sensors while allowing for simulation of atmospheric components, target elevation, gaseous absorption, and Lambertian/anisotropic land surfaces (Vermote E., 2006).

The original purpose of 6Sv was to atmospherically correct land based images, while this project is based upon water targets. Water targets generally reflect a lower percentage of light than those on land, while also introducing much more water vapor into the scene (Jensen, 2007). Unfortunately, in our experimentation comparing ASD on lake and HSI, HICO images processed with 6Sv, we found that 6Sv is not capable of capturing atmospheric variability needed to process scenes for aquatic remote sensing accurately enough to be used as it traditionally is over land. Because of this shortcoming, the empirical line method was used.

2.5.1 Atmospheric Correction of HSI Data

The empirical line method was used to atmospherically correct HSI images. The empirical line method (ELM) uses field measurements of a dark target to compare to the remotely sensed measurements of that same target (Conel et al., 1987). Linear regression between the field-measured and remotely-measured spectra generates a gain and offset curve that is applied to the entire HSI image to produce spectra that closely resembles the field measurements. Ground sampling of a dark reference was taken at the parking lot of Maumee Bay State Park, OH (MBSP) on July 14th and August 11th 2015. On August 11th, NASA GRC coordinated a fly-over of MBSP to coincide with ASD measurements in order to validate the empirical corrections. Since August 11th provided a clear sky day with dry asphalt, any previous or future flyover with similar weather allows for correction using the measurements taken on August 11th. Empirical line corrections were performed in ENVI 5.0, software (Environmental Systems Research Institute).

2.5.2 Atmospheric Correction of HICO Data

The spatial resolution of HICO meant that the small area of MBSP was not suitable for empirical line correction. To counter this, corrected HSI images were used as dark references for the linear regression. On August 15th, 2014, HICO, HSI and ASD measurements were taken. The HSI images were corrected using the technique in section 2.5.1. Five points were selected from the HSI images to use as a dark reference to five points on the HICO image (MB18, 7M, GR1, 4P, and Crib) as these five provided the best results for atmospheric correction.

Table 2.3 Locations and Dates of 2014 Hyperspectral Measurements

Site	Lat (N)	Lon	ASD Dates Collected (2014)	HSI Dates Collected (2014)	HICO Dates (2014)
CRIB	41.68966	-83.27128	7-25, 7-31, 8-7, 8-15, 8-28, 9-15, 9-18, 9-28	8-7, 8-15, 8-18, 8-28, 9-17	8-15, 9-4, 9-8
7M	41.7332	-83.297			
MB18	41.74242	-83.40137			
MB20	41.71563	-83.45483			
8M	41.78947	-83.357			
GR1	41.82082	-83.1845			
4P	41.7498	-83.10368			

Table 2.4 Locations and Dates of 2015 Hyperspectral Measurements on 7 Sample Trip

Site	Lat (N)	Lon	ASD Dates Collected (2015)	HSI Dates Collected (2015)
CRIB	41.68966	-83.27128	7-1, 7-27, 8-10, 9-8	7-14, 8-10, 8-24, 9-8, 9-21, 9-28, 10-5
7M	41.7332	-83.297		
MB18	41.74242	-83.40137		
MB20	41.71563	-83.45483		
8M	41.78947	-83.357		
GR1	41.82082	-83.1845		
4P	41.7498	-83.10368		

Table 2.5 Locations and Dates of 2015 Hyperspectral Measurements on EW Sample Trip

Site	Lat (N)	Long	ASD Dates Collected (2015)	HSI Dates Collected (2015)
EW1	41.68966	-83.27128	7-20, 8-4, 8-17	7-20, 7-27, 8-17
EW2	41.715	-83.278		
EW3	41.7332	-83.297		
EW4	41.728	-83.336		
EW5	41.725	-83.37		

2.6 Algae Retrieval Algorithms

In order to determine the best algal retrieval algorithm to use, a comparison of commonly used algorithms was performed. Background information of each algorithm used is described below, results of the comparison are provided in chapter 3.

2.6.1 The Simis and Randolph Algorithms

First developed in 2005 by Simis, and improved upon by Randolph in 2008, these equations (eqs. 1 – 4 of table 2.6) are meant to remotely sense the concentration of Phycocyanin (Randolph et al., 2008; Simis et al., 2005). Backscatter values were found using Randolph's equation (Table 2.6, eq 1) and then applied to the Simis equations (Table 2.6, eqs 2, 3). Coefficients used in equations of table 4.4 are located in table 2.7, values were derived from multiple efforts by Astoreca, Gons, and Gordon (Astoreca et al., 2006; Gons, 1999; Gordon et al., 1988). Coefficients of absorption of water at various wavelengths was found by Buiteveld et al. (Buiteveld et al., 1994).

The absorption coefficient of Phycocyanin (a*PC(620)) was found by dividing the measured absorption of Phycocyanin at 620 nm by the measured concentration of cyanobacteria from a water sample. Due to the fact that measurements were taken at seven sample sites, the values of concentration and absorption were averaged over these seven sites, and the resultant value was used as (a*PC(620)) for all calculations.

The process of calculating derived concentration of Phycocyanin is shown in Table 2.6, equations 1-4.

Table 2.6. Equations used for Algal Retrieval Comparison

Equation	Source
(1) $b_b = [a_w(778) \cdot \alpha \cdot \mathrm{R}(778)] \cdot [\gamma' - \alpha \cdot \mathrm{R}(778)]^{-1}$	Randolph et al.
(2) $a_{chl}(665) = \Bigg(\Bigg\{\Bigg[\frac{R(709)}{R(665)} \cdot (a_w(709) + b_b)\Bigg\} - b_b - a_w(665)\Bigg) \cdot \gamma^{-1}$	Simis et al.
(3) $a_{PC}(620) = \Bigg(\Bigg\{\Bigg[\frac{R(709)}{R(620)} \cdot (a_w(709) + b_b)\Bigg\} - b_b - a_w(620)\Bigg) \cdot \delta^{-1} - [\varepsilon \cdot a_{chl}(665)]$	Simis et al.
(4) $[PC] = \frac{a_{PC}(620)}{a *_{PC} (620)}$	Simis et al.
(5) $SS_{(681)} = R(681) - R(665) - \{R(709) - R(665)\} \cdot \left(\frac{681 - 665}{709 - 665}\right)$	Wynne et al.
(6) $CI = -SS_{(681)}$	Wynne et al.

Table 2.7. Constants and coefficients used in the Simis and Randolph algorithms

Constant	**Meaning**	**Value**
aw(620)	Absorption coefficient of water at 620 nm (m^-1)	0.281
aw(665)	Absorption coefficient of water at 665 nm (m^-1)	0.401
aw(709)	Absorption coefficient of water at 709 nm (m^-1)	0.727
aw(778)	Absorption coefficient of water at 778 nm (m^-1)	2.71
γ	Correction factor for a(665)	0.68
δ	Correction factor for a(620)	0.84
ε	Conversion factor used to relate absorbencies by chl-a at 665 and 620 nm	0.24
α	Correction factor for surface refraction	0.60
γ’	Experimental factor	0.082
a*PC(620)	Specific absorption coefficient of water at 620nm (m^-1)	0.03408752

2.6.2 Validation of CI with ASD Readings

Cyanobacteria Index (CI) maps were produced from HSI and HICO images and compared to measured cyanobacteria concentration to validate the algorithm using eq. 4. Sampling points for validation were chosen on dates August 10th and September 8th, 2015 as these dates featured coincident datasets of airborne and on-lake measurements during the bloom period. Points were selected from these dates which had no surface scum present. The CI technique requires that surface scum is absent from the point of interest in order to correlate with measured cyanobacteria as the cyanobacteria measurement uses a water sample averaged through the water column, while reflectance takes place at the surface. Seven sampling points met these criteria. Cyanobacteria concentration was plotted against the CI and the linear correlation was tested via R^2 value.

2.6.3 Validation of CI with HSI readings

Again the dates August 10th and September 8th, 2015 were chosen. Six sample points met the criteria. Cyanobacteria concentration was plotted against the CI and the correlation was tested via R^2 value.

2.6.4 Validation of CI with HICO readings

Sampling points for validation were taken from August 15th, 2014. All seven sampling sites met the comparison criteria. Cyanobacteria concentration was plotted against the CI and the correlation was tested via R^2 value.

Chapter 3

Results

3.1 Overview of Results

The purpose of this investigation was to test atmospheric correction techniques and algae retrieval algorithms to improve methods leading to mapping of HABs in WLE. The results of the investigation are as follows.

3.2 Results of Atmospheric Correction

The empirical line method (ELM) was used to atmospherically correct airborne and satellite images in this investigation. Correction of these images proved to be effective as visual analysis of the pre- and post-correction spectra to ground measurements show that spectral signatures of algae were preserved in the data (Figures 3-2 and 3-3).

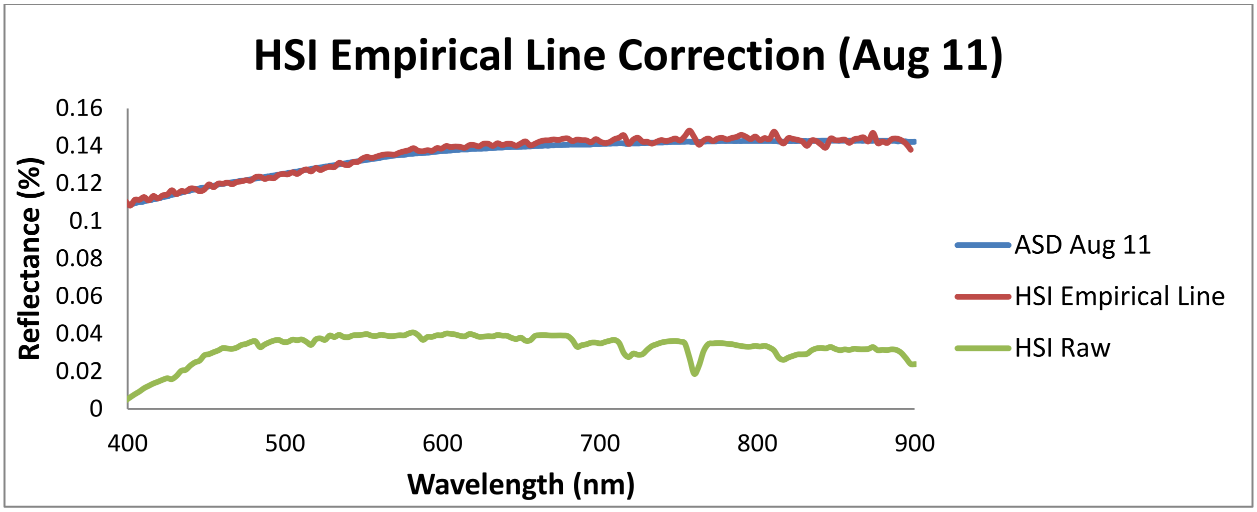

Figure 3-1 ELM correction over MBSP parking lot showing effectiveness of the correction technique. Green line is raw HSI data, red is the ELM corrected data, and blue is ASD ground measured data.

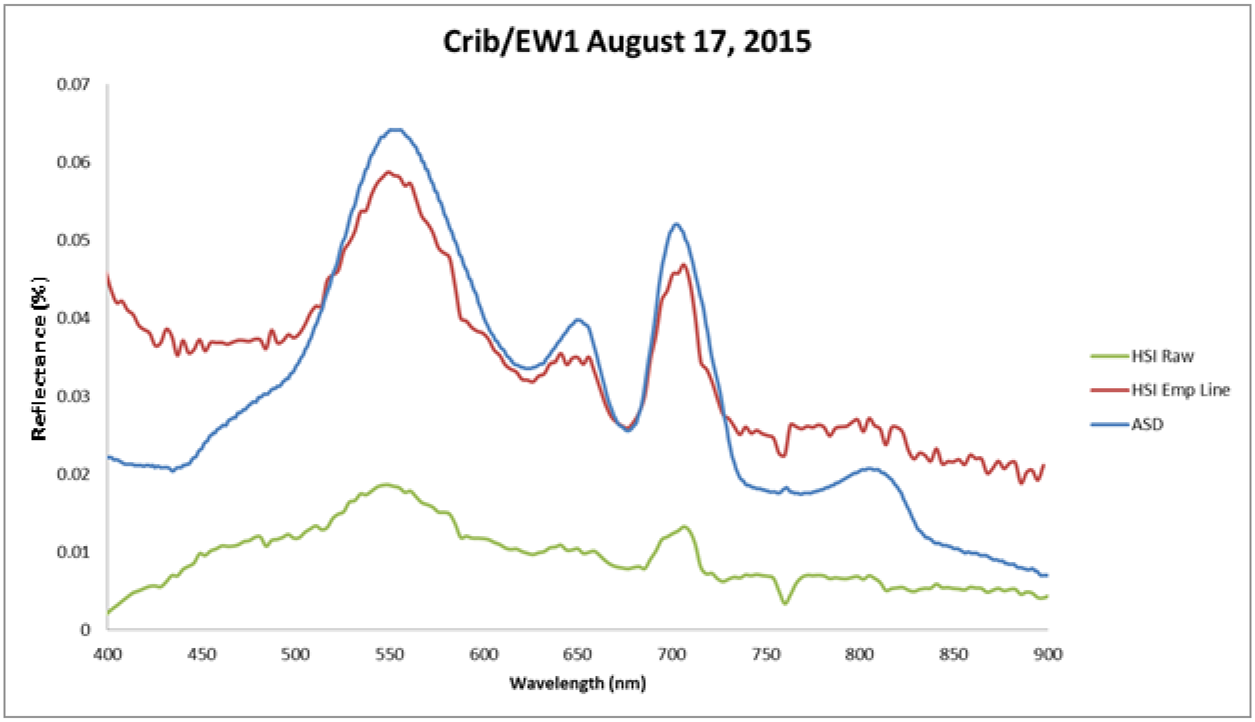

Figure 3-2 ELM correction over CRIB on August 17, 2015 as an example of correction over algae laden water. Green line is raw HSI data, red is the ELM corrected data, and blue is ASD ground measured data.

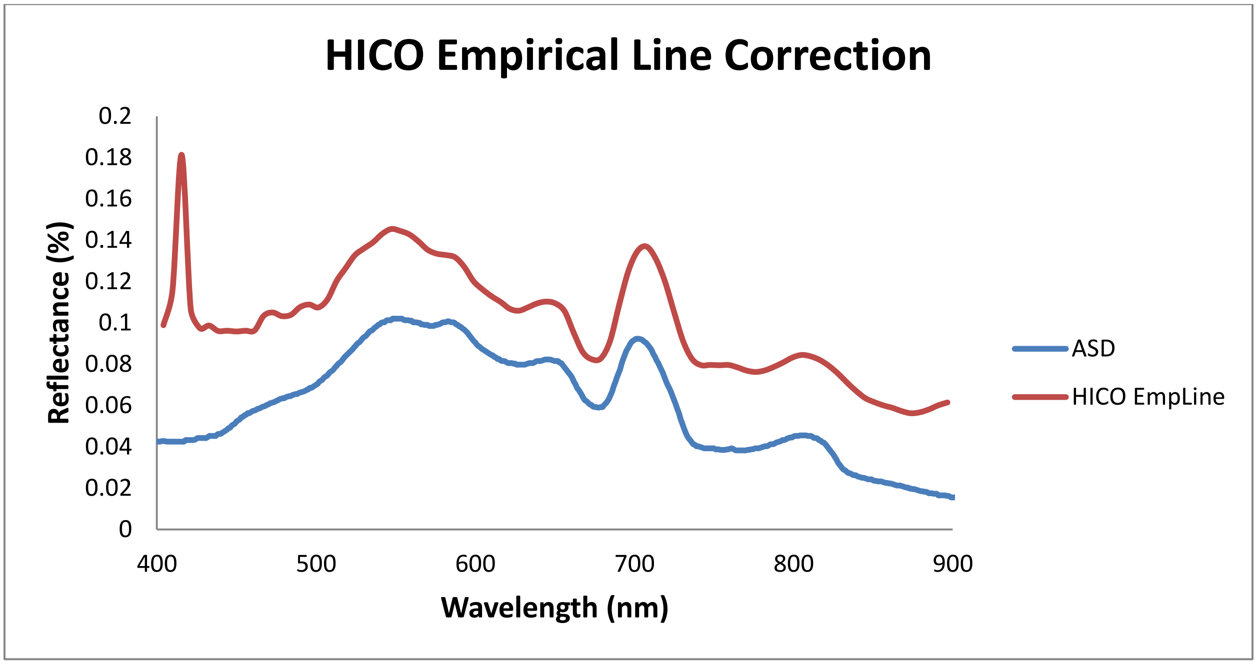

Figure 3-3 ELM correction for HICO on August 15, 2014 over CRIB. Red is ELM corrected HICO image and blue is ground measured data. Raw HICO data is not included in order to better display differences between corrected data and ground reference.

3.3 Comparison of Algae Retrieval Algorithms

In order to determine which algorithm is best suited for this project, bloom maps were generated for each algorithm from HSI and HICO images, and compared to measured cyanobacteria concentration. ASD measurements were also run through each algorithm to validate each at the ground level.

Derived Phycocyanin concentrations and CI values were separated into “remotely sensed” (HSI and HICO) and “ground level” (ASD) and plotted against measured cyanobacteria concentration. The values calculated for each algorithm using remotely sensed data and the measured cyanobacteria concentrations are located in tables 3.1 and 3.2. The resultant graphs plotted coefficient of determination (R^2) values which were used to compare accuracy of each algorithm. The resulting values are found in table 3.3.

Table 3.1. Comparison of Simis derived Phycocyanin concentrations (m^2*mg pigment^{-1}) to in lake measured cyanobacteria concentrations, including site names and locations. (Chelpon et al. 2015)

Site	Latitude (N)	Longitude (W)	Measured Blue-Green Algae Concentration (mcg/L)	ENVI Derived [PC] (HSI)	ENVI Derived [PC] (HICO)
GR1	41.82082	-83.1845	1.94625		5.695701606
4P	41.7498	-83.10368	3.9475		0.592188178
8M	41.78947	-83.357	7.81		7.779399423
7M	41.7332	-83.297	23.135		13.37229271
CRIB	41.68966	-83.27128	25.94125		16.62826421
MB18	41.74242	-83.40137	25.0525	8.632781	16.79807618
MB20	41.71563	-83.45483	26.83	-4.04077	27.84627391

Table 3.2. Comparison of Wynne derived Cyanobacteria Index to in lake measured cyanobacterial concentration, including site names and locations. (Chelpon et al. 2015)

Site	Latitude (N)	Longitude (W)	Measured Blue-Green Algae Concentration (mcg/L)	ENVI Derived CI (HSI)	ENVI Derived CI (HICO)
GR1	41.82082	-83.1845	1.94625		-0.003042
4P	41.7498	-83.10368	3.9475		0.000009
8M	41.78947	-83.357	7.81		0.007643
7M	41.7332	-83.297	23.135		0.011911
CRIB	41.68966	-83.27128	25.94125		0.021558
MB18	41.74242	-83.40137	25.0525	0.018328	0.013035
MB20	-83.45483	41.71563	26.83	0.006619	0.011212

Table 3.3. R^2 values of Simis and Wynne algorthims comparing their products of ground based and remotely sensed measurements to cyanobacteria concentration. (Chelpon et al. 2015)

Method	R^2 Value
Simis et al. using ground reference data	0.7683
Wynne et al. using ground reference data	0.7784
Simis et al. using remotely sensed data	0.4956
Wynne et al. using remotely sensed data	0.7794

3.3.1 Results of Algae Retrieval Algorithm Comparison

Ground level calculations for both Simis and Wynne algorithms yielded favorable results with R^2 values of 0.7683 and 0.7784 (Figures 3-4 and 3-5), respectively. Applying each algorithm to remotely sensed data produced troubling results for the Simis algorithm.

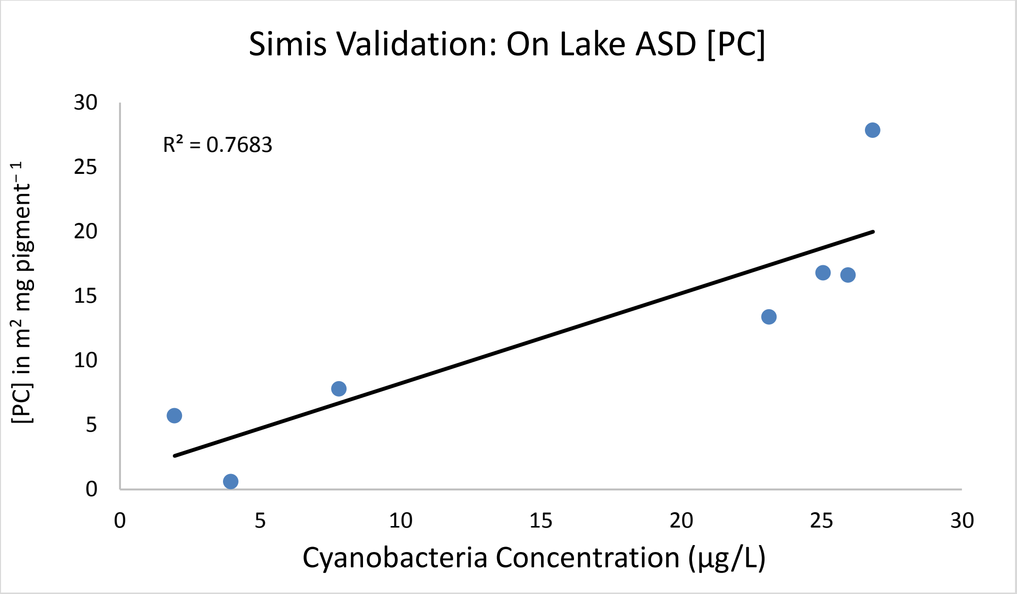

Figure 3-4. Simis method validation for on-lake ASD measurements compared to fluoroprobe measured cyanobacteria concentrations (Chelpon et al. 2015)

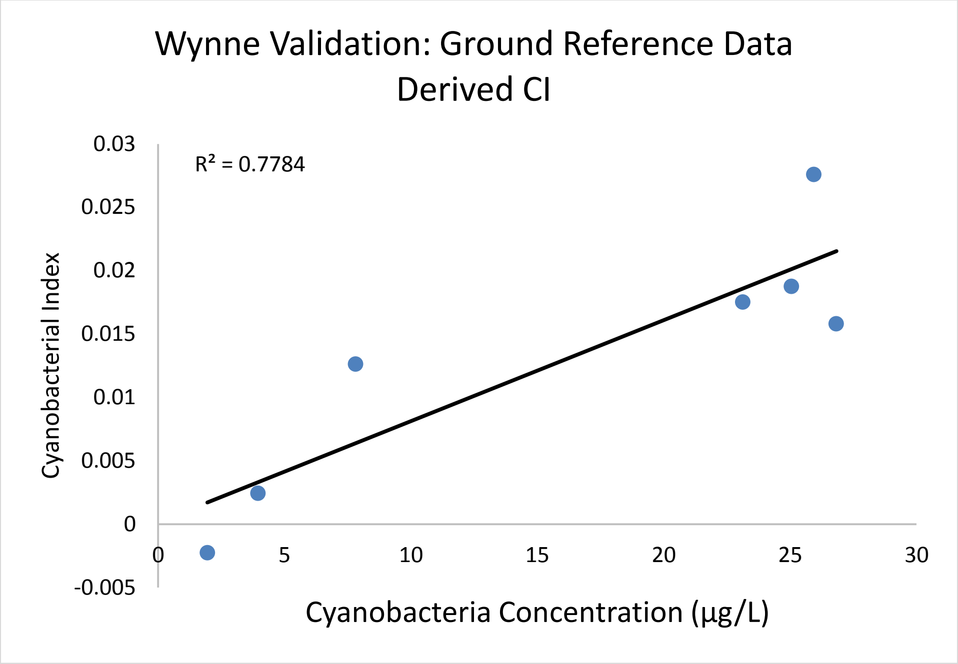

Figure 3-5. Wynne CI validation for on-lake ASD measurements compared to fluoroprobe measured cyanobacteria concentrations (Chelpon et al. 2015).

The Simis method produced a remotely sensed R^2 of just 0.4956 (Figure 3-6), due to a lack of correlation between points GR1 and 4P of the HICO image to measured cyanobacteria and no correlation at all between HSI and HICO derived Phycocyanin concentrations for points MB18 and MB20. This is most likely due to sensitivity to atmospheric correction problems as the HSI value for MB20 was negative, invalidating the Simis technique for this investigation.

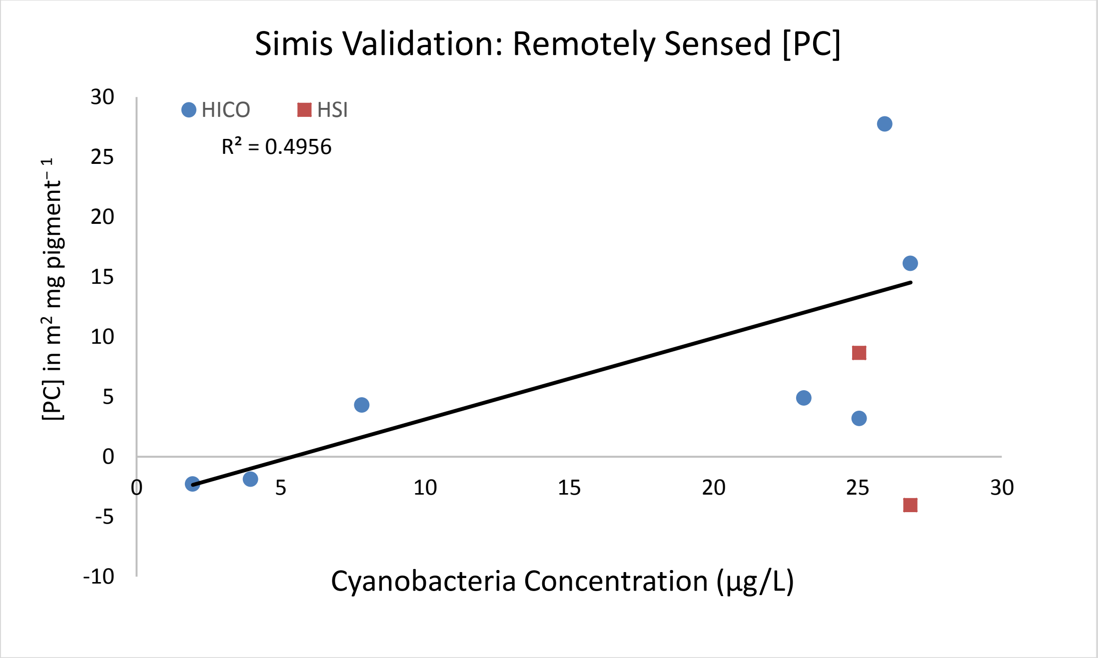

Figure 3-6. Simis method validation for remotely sensed HICO and HSI data compared to fluoroprobe measured cyanobacteria concentrations (Chelpon et al. 2015).

The remotely sensed Wynne method generated a much stronger correlation to measured cyanobacteria concentration than the Simis method (R^2 of 0.7794, figure 3-7). Unlike the Simis technique, CI values correlate very well to the HSI points MB18 and MB20, which demonstrates the insensitivity to atmospheric correction errors that the spectral shape algorithm is capable of.

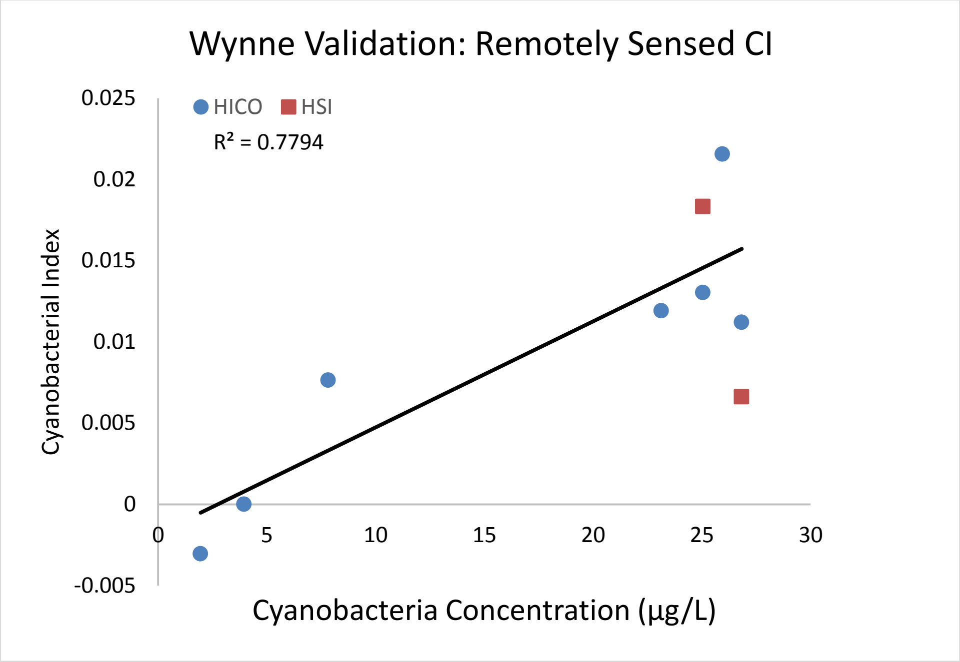

Figure 3-7. Wynne method validation for remotely sensed HICO and HSI data compared to measured cyanobacteria concentrations (Chelpon et al. 2015).

3.4 Results of Cyanobacteria Index

The Wynne Cyanobacteria Index was used on ASD ground measurements and compared to measured cyanobacteria concentration in order to determine its effectiveness in western Lake Erie, and shows a very strong correlation (Figure 3-8). HSI and HICO derived CI were compared to measured cyanobacteria concentration in the same way in order to determine CI's effectiveness for remotely sensed imagery, which also show strong correlation (Figures 3-9, 3-10). Points selected for this comparison were chosen because they were flown coincidentally to on-lake measurements, occurred during a significant algal bloom, and were not in an area dominated by surface scum.

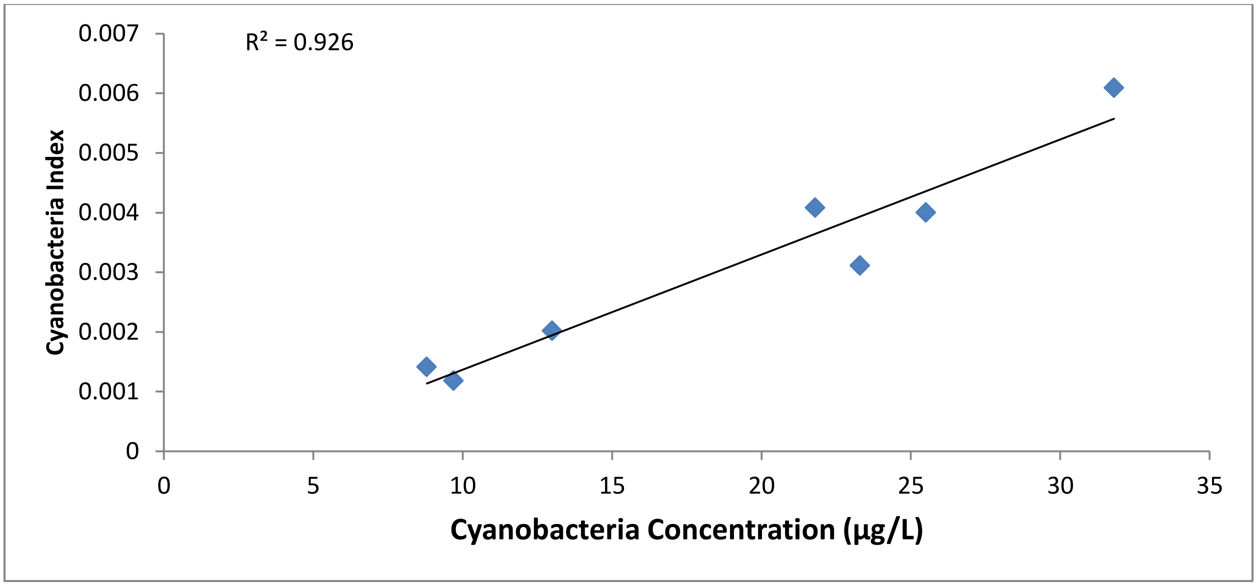

Figure 3-8 Comparison of fluoroprobe measured cyanobacteria concentration to ASD derived CI. Points that met the criteria were selected from August 10 and September 08, 2015.

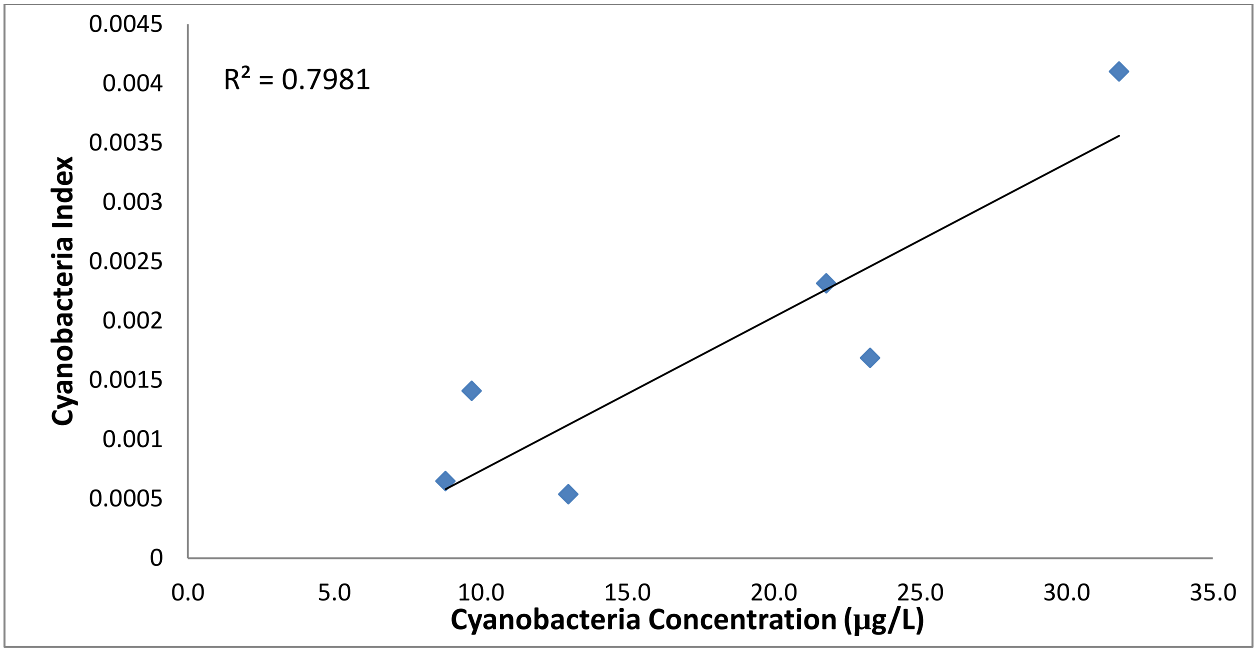

Figure 3-9 Comparison of fluoroprobe measured cyanobacteria concentration to HSI derived CI. Points that met the criteria were selected from August 10 and September 08, 2015.

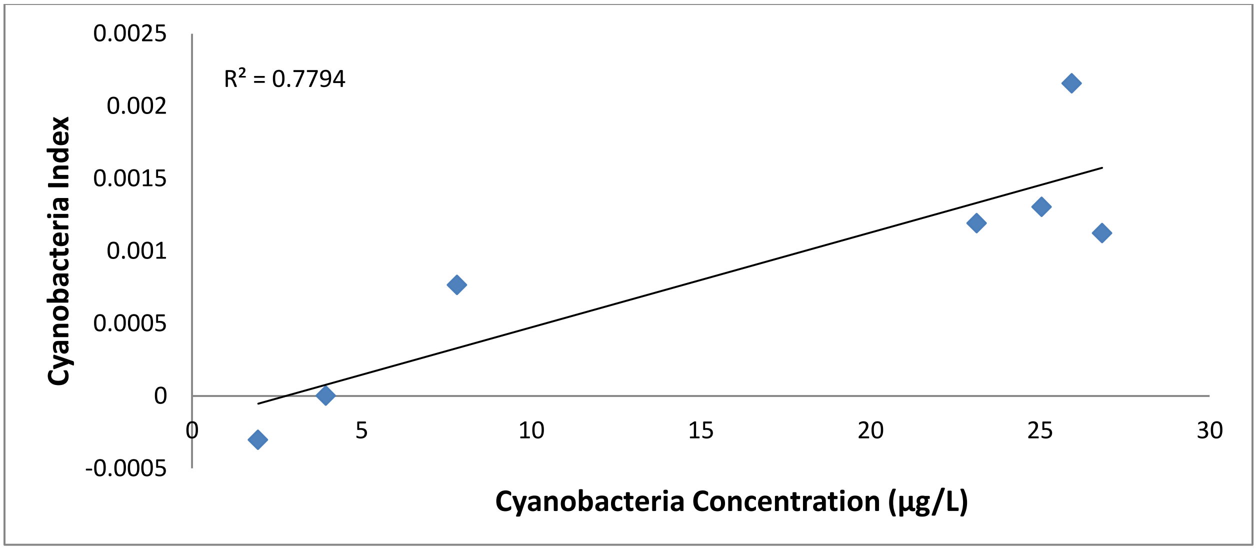

Figure 3-10 Comparison of fluoroprobe measured cyanobacteria concentration to HICO derived CI. Points that met the criteria were selected from August 15, 2014.

3.5 Time Series of Cyanobacteria Index

A time series of the 2015 HSI HAB monitoring images are shown below in figures 3-11 – 3-14. All images are flown over the Toledo water intake (Crib). Figure 3-11 depicts a single band (555 nm) of the HSI image with no processing performed. Due to the nature of CI being relative to surrounding pixels in the same image, two different thresholds of CI are depicted in figures 3-12 and 3-13. Figure 3-12 has a lower CI threshold, a maximum of 0.01, while figure 3-13 has a larger threshold of 0.07. The differing thresholds are necessary to show the progress of the bloom in a high level of detail, without washing out of extreme low or high values using one threshold would produce. Figure 3-14 depicts the most prevalent bloom day, August 10, 2015, as both a single band image (555 nm) and as a CI image with a threshold of 0.07. Note that the boat track shown in figure 3-10 indicates a shallow bloom, as the recent water turn over from the boat's wake generates a much lower CI than the surrounding bloom area.

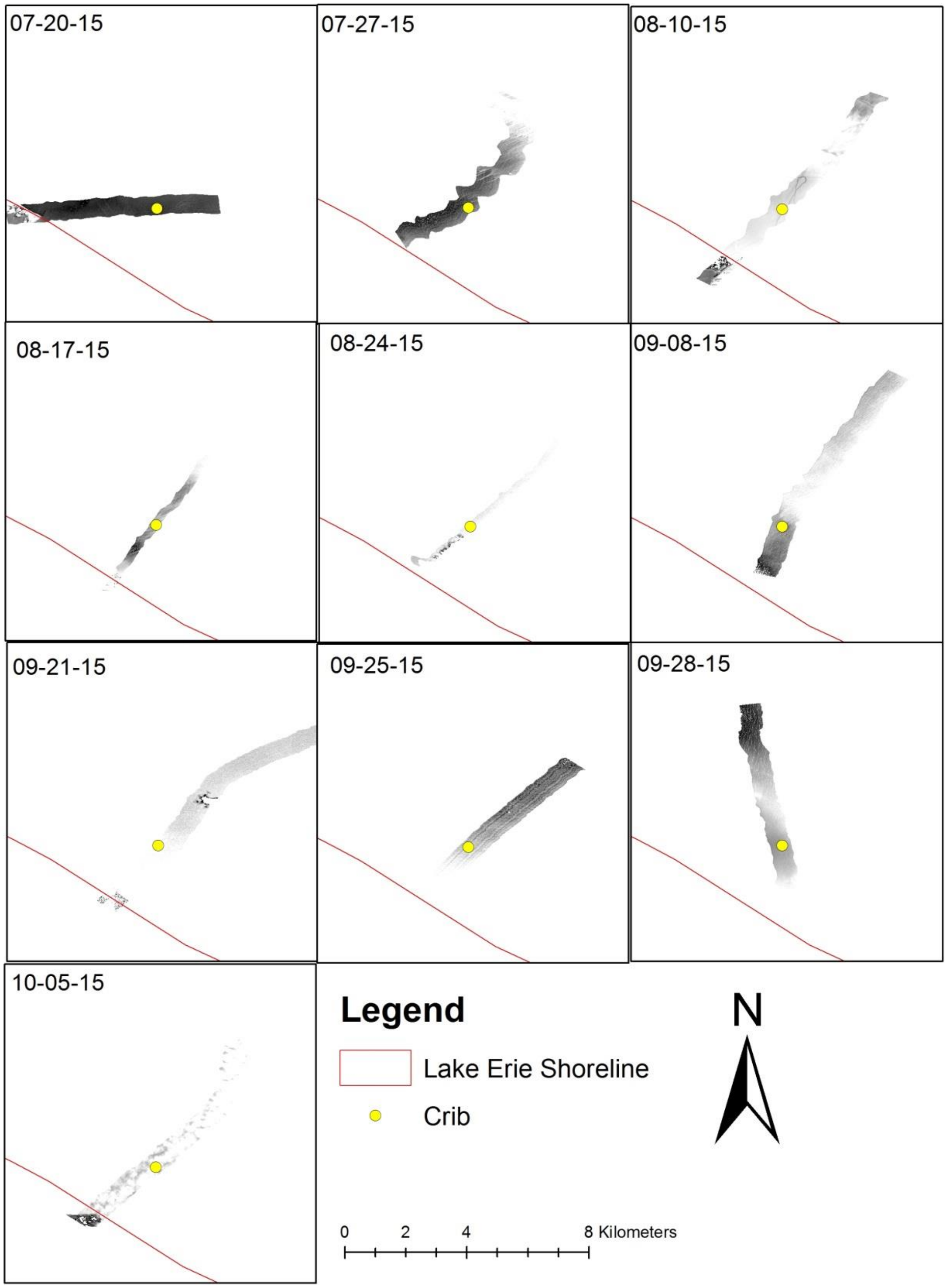

Figure 3-11 Time Series of single band HSI images over the Crib progressing through 2015. Red line indicates Lake Erie shoreline, yellow dot indicates location of the Crib.

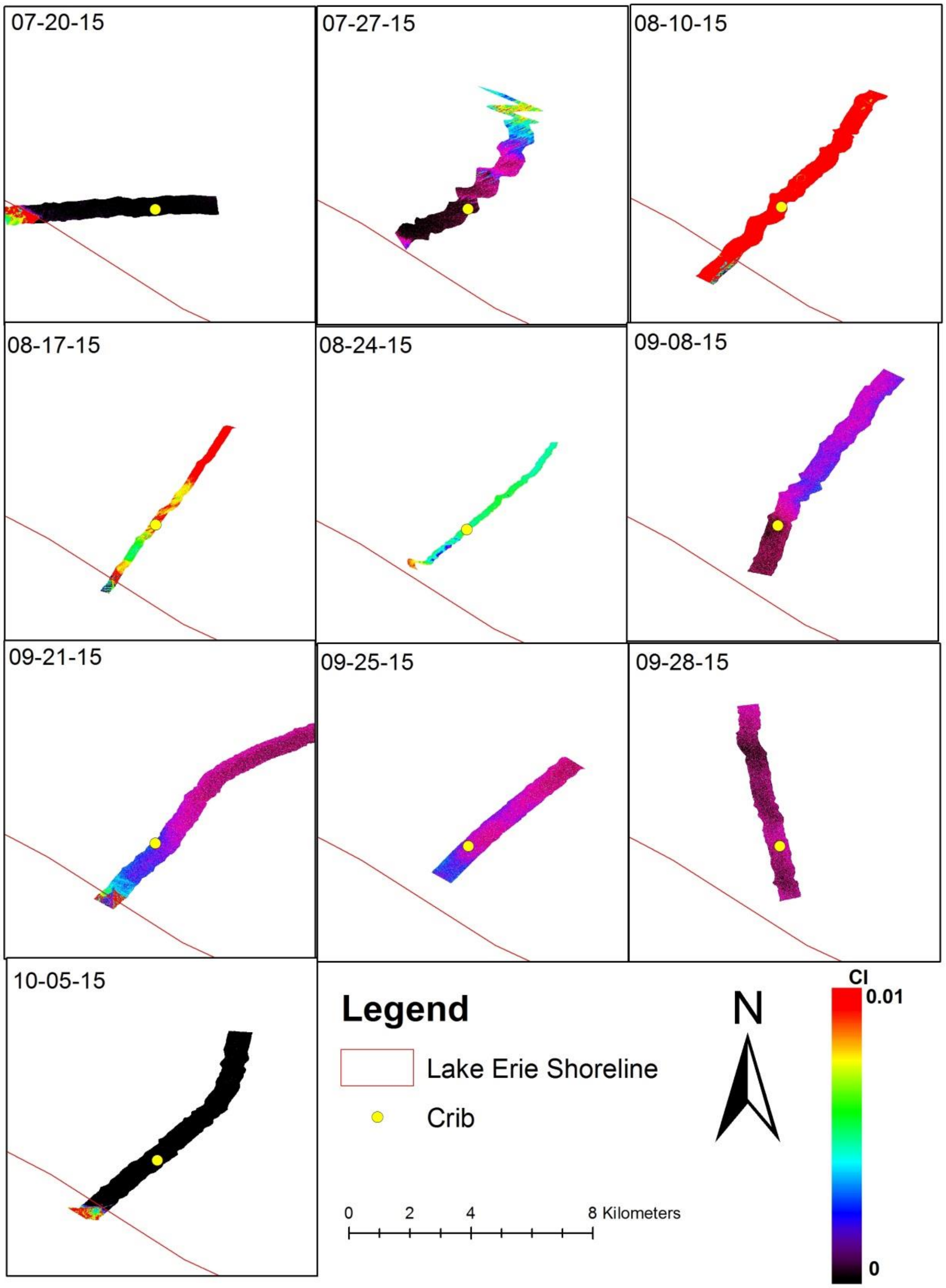

Figure 3-12 Time Series of HSI derived CI images over the Crib progressing through 2015 using a CI threshold of 0.01. Red line indicates Lake Erie shoreline, yellow dot indicates location of the Crib.

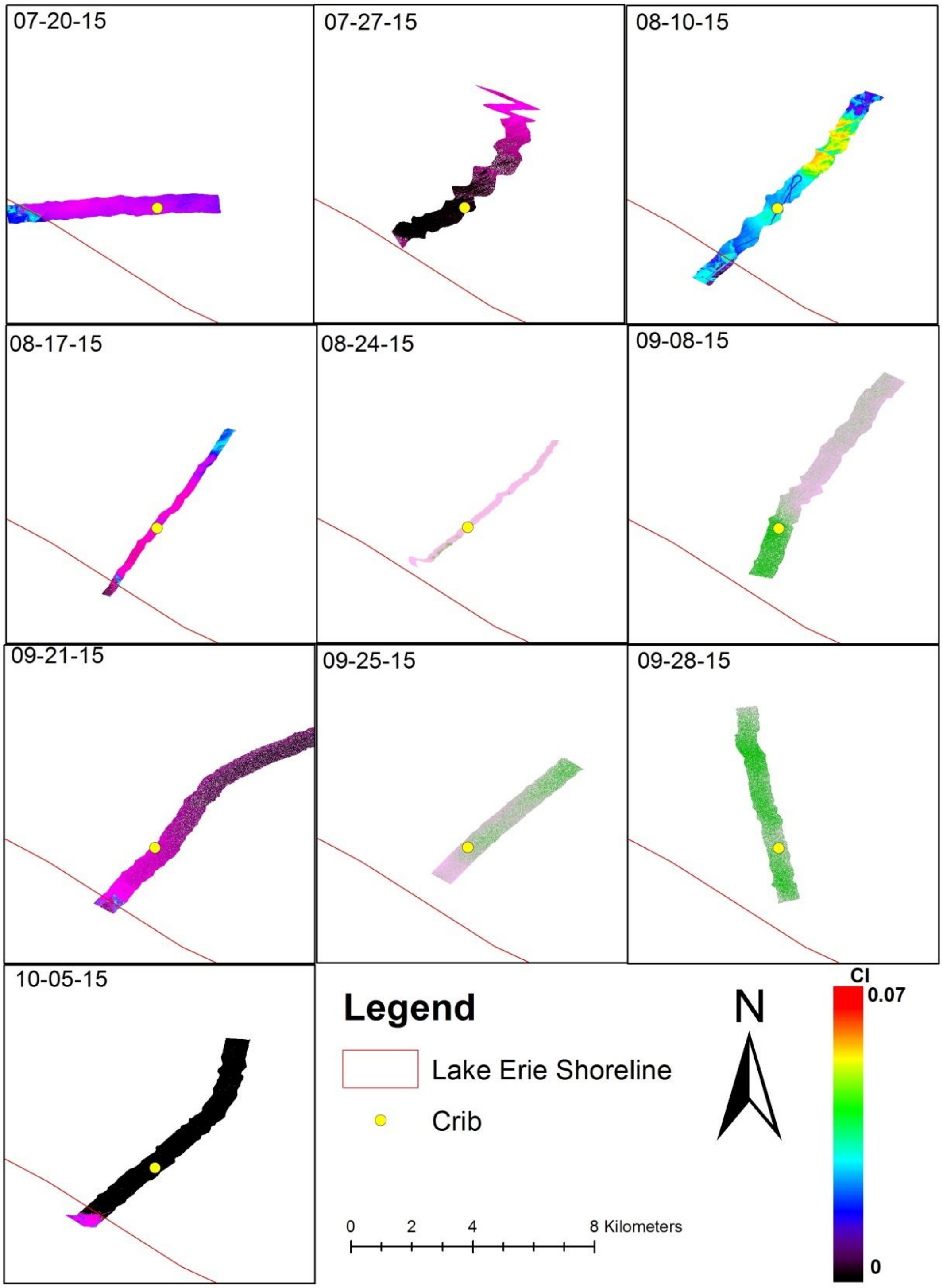

Figure 3-13 Time Series of HSI derived CI images over the Crib progressing through 2015 using a CI threshold of 0.07. Red line indicates Lake Erie shoreline, yellow dot indicates location of the Crib.

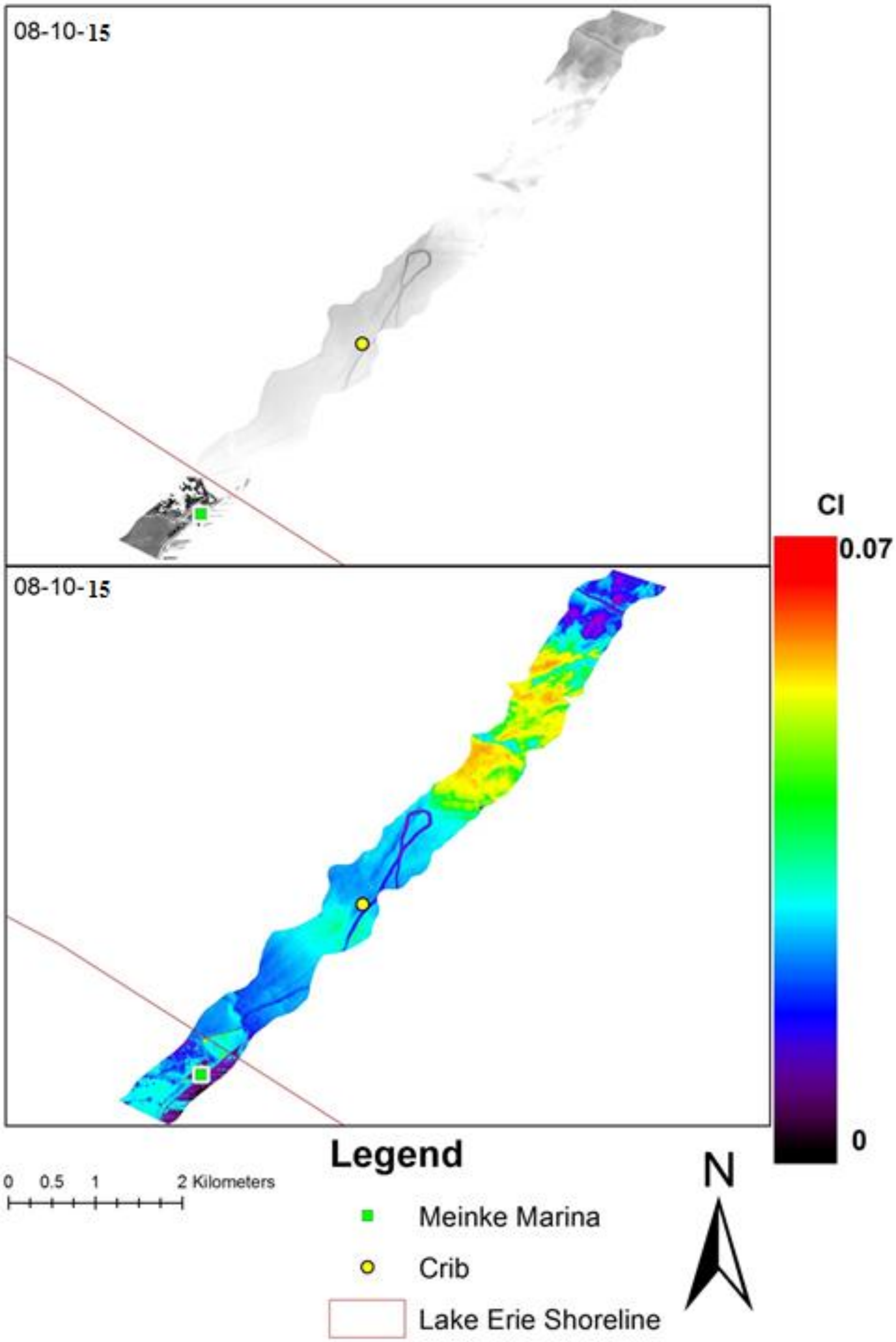

Figure 3-14 Close-up of HSI derived CI image over the Crib for August 10, 2015 using a CI threshold of 0.07. Red line indicates Lake Erie shoreline, yellow dot indicates location of the Crib, green square indicates Meinke Marina.

Chapter 4

Discussion and Conclusion

4.1 Discussion of Atmospheric Correction Techniques

Due to the short comings of the 6Sv algorithm, the empirical line method was used. The empirical line technique allowed for very accurate correction of airborne and satellite images, but does lack the automation that 6Sv offers. The empirical line method (ELM) requires that the HSI be flown over Maumee Bay State Park on each day that samples were taken, in order to correct images for that day, adding an additional flight path to an already packed schedule. Additionally, ELM could not be entirely automated because cloud cover can obscure the dark target, the parking lot of MBSP, via shadowing and result in over correction of the image. Another issue of ELM is that the spatial resolution of HICO meant that MBSP's parking lot contained mixed pixels and could not be used to directly correct for atmospheric interference.

Shortcomings of ELM were able to be circumvented, however. NASA GRC found no issue in flying over MBSP on sample days as it was imperative to the research. Only once did cloud cover obscure the middle parking lot of MBSP, and in this unique case, measurements of the northern lot were used for corrections and provided excellent results. In order to correct the HICO image, coincident HSI images were corrected first using the standard ELM method. These corrected images were then used as reference targets in place of the MBSP parking lot, and correction results were satisfactory.

4.2 Issues of Data Collection

This investigation dealt with an immense amount of data collection; satellite, airborne, and on-lake hyperspectral measurements coupled with lab analysis of water samples, all performed by a large team of dedicated scientists. With such a large and complex set of data collection, issues were bound to occur. Measurements taken on the lake were entirely dependent on the weather; large waves kept the research vessels off the lake and cut sampling trips short multiple times. Wind and waves also disrupted the research vessel's anchored location, pushing it off location slightly, or in the case of being anchored near a structure like the Toledo water intake, forcing a different location altogether. These occurrences were rarities however, and for the most part, the vessel was anchored on the correct location.

While the NASA GRC pilots were highly skilled, there was trouble in flying over exactly where the research vessel was located. Complicating factors for taking a precise measurement include the aircraft speed, elevation, and high spatial resolution of the sensor used, which all together makes flying over a specific target (one as small as a single GPS point in a large body of water) a difficult task. Again, these problems were a rarity and due to the highly skilled flight teams, the targets were hit more often than not.

The nature of algae blooms provided their own complications to on lake sampling. When algae groups grow in calm waters, they form a surface scum. This scum generates a high reflectance in the green spectrum, giving remotely sensed observations a type of false positive for algal abundance. A false positive is problematic because cyanobacteria concentrations are measured through the water column as an average, so while the remote sensing reflectance gives high values (and thus a high CI), the actual amount of algae beneath the scum is generally much lower. Algal blooms also exhibit features known as “streamers”; long, thin strands of algae surface scum which further complicate target measurements from both the ground and airborne perspective as a difference of a meter can impact weather the measurement is surface scum or not.

4.3 Conclusions

The goals of this project were to improve the methodology leading to mapping of harmful algal blooms in Lake Erie’s western basin by way of remote sensing. In order to do this, remotely sensed images were atmospherically corrected via ELM techniques, as this proved to be the most useful atmospheric correction technique. Various algal retrieval algorithms were tested in order to map HABs, and the Wynne CI (2010) algorithm proved to be the most useful. Results from the Wynne Cyanobacterial Index were compared to on-lake sample data, using points that fell on coincident dates of NASA GRC HSI flyovers and one HICO image using measured cyanobacteria concentrations on areas which did not exhibit surface scum. This investigation shows that hyperspectral remote sensing can be used to identify harmful algal blooms in Case 2 waters, like those of western Lake Erie.

References

Aiken, J., Moore, G., Trees, C., Hooker, S., and Clark, D., 1996, The SeaWiFS CZCS-type pigment algorithm: Oceanographic Literature Review, v. 3, no. 43, p. 315-316.

Astoreca, R., Ruddick, K., Rousseau, V., Van Mol, B., Parent, J.-Y., and Lancelot, C., 2006, Variability of the inherent and apparent optical properties in a highly turbid coastal area: impact on the calibration of remote sensing algorithms: EARSeL eProceedings, v. 5, no. 1, p. 1-17.

Azevedo, S. M., Carmichael, W. W., Jochimsen, E. M., Rinehart, K. L., Lau, S., Shaw, G. R., and Eaglesham, G. K., 2002, Human intoxication by microcystins during renal dialysis treatment in Caruaru—Brazil: Toxicology, v. 181, p. 441-446.

Benner, R., and Kaiser, K., 2011, Biological and photochemical transformations of amino acids and lignin phenols in riverine dissolved organic matter: Biogeochemistry, v. 102, no. 1-3, p. 209-222.

Berk, A., Bernstein, L. S., and Robertson, D. C., 1987, MODTRAN: A moderate resolution model for LOWTRAN: DTIC Document.

Brady, N. C., and Weil, R. R., 2008, Soil water: Characteristics and behavior: The nature and properties of soils. Prentice Hall, New Jersey, p. 177-217.

Bridgeman, T. B., 2006, MAUMEE BAY AND WESTERN LAKE ERIE WATER QUALITY MONITORING.

Bridgeman, T. B., Chaffin, J. D., and Filbrun, J. E., 2013, A novel method for tracking western Lake Erie< i> Microcystis</i> blooms, 2002–2011: Journal of Great Lakes Research, v. 39, no. 1, p. 83-89.

Buiteveld, H., Hakvoort, J., and Donze, M., Optical properties of pure water, *in* Proceedings Ocean Optics XII1994, International Society for Optics and Photonics, p. 174-183.

Bukata, R. P., Jerome, J. H., Kondratyev, A. S., and Pozdnyakov, D. V., 1995, Optical properties and remote sensing of inland and coastal waters, CRC press.

Carder, K. L., Steward, R. G., Harvey, G. R., and Ortner, P. B., 1989, Marine humic and fulvic acids: Their effects on remote sensing of ocean chlorophyll: Limnology and oceanography, v. 34, no. 1, p. 68-81.

CGLP, 1977, Cornwall, Ontario: Coordinating Committee on Great Lakes Basic Hydraulic and Hydrologic Data.

Chorus, I., and Bartram, J., 1999, Toxic cyanobacteria in water: A guide to their public health consequences, monitoring and management, Spon Press.

Conel, J. E., Green, R. O., Vane, G., Bruegge, C. J., Alley, R. E., and Curtiss, B. J., 1987, AIS-2 radiometry and a comparison of methods for the recovery of ground reflectance.

Gitelson, A., 1992, The peak near 700 nm on radiance spectra of algae and water: relationships of its magnitude and position with chlorophyll concentration: International Journal of Remote Sensing, v. 13, no. 17, p. 3367-3373.

Gons, H. J., 1999, Optical teledetection of chlorophyll a in turbid inland waters: Environmental Science & Technology, v. 33, no. 7, p. 1127-1132.

Gordon, H. R., Brown, O. B., Evans, R. H., Brown, J. W., Smith, R. C., Baker, K. S., and Clark, D. K., 1988, A semianalytic radiance model of ocean color: Journal of Geophysical Research: Atmospheres, v. 93, no. D9, p. 10909-10924.

Han, L., 1997, Spectral reflectance with varying suspended sediment concentrations in clear and algae-laden waters: Photogrammetric Engineering and Remote Sensing, v. 63, no. 6, p. 701-705.

Han, L., and Rundquist, D. C., 1997, Comparison of NIR/RED ratio and first derivative of reflectance in estimating algal-chlorophyll concentration: A case study in a turbid reservoir: Remote sensing of Environment, v. 62, no. 3, p. 253-261.

Hargreaves, B. R., 2003, Water column optics and penetration of UVR: UV effects in aquatic organisms and ecosystems, v. 1, p. 59-108.

Hudnell, H. K., and Dortch, Q., 2008, A synopsis of research needs identified at the interagency, international symposium on cyanobacterial harmful algal blooms (ISOC-HAB), Cyanobacterial Harmful Algal Blooms: State of the Science and Research Needs, Springer, p. 17-43.

Jensen, J., 2007, Remote Sensing of the Environment: An Earth Resource Perspective: Pearson Prentice Hall: Upper Saddle River, NJ.

Kotchenova, S. Y., Vermote, E. F., Matarrese, R., and Klemm Jr, F. J., 2006, Validation of a vector version of the 6S radiative transfer code for atmospheric correction of satellite data. Part I: Path radiance: Applied optics, v. 45, no. 26, p. 6762-6774.

Lucke, R. L., Corson, M., McGlothlin, N. R., Butcher, S. D., Wood, D. L., Korwan, D. R., Li, R. R., Snyder, W. A., Davis, C. O., and Chen, D. T., 2011, Hyperspectral Imager for the Coastal Ocean: instrument description and first images: Applied Optics, v. 50, no. 11, p. 1501-1516.

Michalak, A. M., Anderson, E. J., Beletsky, D., Boland, S., Bosch, N. S., Bridgeman, T. B., Chaffin, J. D., Cho, K., Confesor, R., and Daloğlu, I., 2013, Record-setting algal bloom in Lake Erie caused by agricultural and meteorological trends consistent with expected future conditions: Proceedings of the National Academy of Sciences, v. 110, no. 16, p. 6448-6452.

MichiganSeaGrant, 2006, Michigan Sea Grant.

Mobley, C., 2010, Overview of Optical Oceanography.

Morel, A., and Prieur, L., 1977, Analysis of variations in ocean color: Limnology and oceanography, v. 22, no. 4, p. 709-722.

NASA, 2016, Landsat Science History: From the Begining, Volume 2016.

Preisendorfer, R. W., 1976, Hydrologic Optics. Volume 5. Properties: Honolulu: US Dept. of Commerce, National Oceanic and Atmospheric Administration, Environmental Research Laboratories, Pacific Marine Environmental Laboratory.

Randolph, K., Wilson, J., Tedesco, L., Li, L., Pascual, D. L., and Soyeux, E., 2008, Hyperspectral remote sensing of cyanobacteria in turbid productive water using optically active pigments, chlorophyll a and phycocyanin: Remote Sensing of Environment, v. 112, no. 11, p. 4009-4019.

Reche, I., Pace, M. L., and Cole, J. J., 1999, Relationship of trophic and chemical conditions to photobleaching of dissolved organic matter in lake ecosystems: Biogeochemistry, v. 44, no. 3, p. 259-280.

Rundquist, D. C., Schalles, J. F., and Peake, J. S., 1995, The response of volume reflectance to manipulated algal concentrations above bright and dark bottoms at various depths in an experimental pool: Geocarto international, v. 10, no. 4, p. 5-14.

Sathyendranath, S., 2000, Reports of the International Ocean-Colour Coordinating Group: IOCCG, Dartmouth, Canada, v. 3, p. 140.

Shuchman, R. A., Leshkevich, G., Sayers, M. J., Johengen, T. H., Brooks, C. N., and Pozdnyakov, D., 2013, An algorithm to retrieve chlorophyll, dissolved organic carbon, and suspended minerals from Great Lakes satellite data: Journal of Great Lakes Research, v. 39, p. 14-33.

Simis, S. G., Peters, S. W., and Gons, H. J., 2005, Remote sensing of the cyanobacterial pigment phycocyanin in turbid inland water: Limnology and Oceanography, v. 50, no. 1, p. 237-245.

Stumpf, R. P., Wynne, T. T., Baker, D. B., and Fahnenstiel, G. L., 2012, Interannual variability of cyanobacterial blooms in Lake Erie: PLoS One, v. 7, no. 8, p. e42444.

Traub, J., 2012, Patterns in the variation of CDOM spectral slopes in the Western Lake Erie Basin: University of Toledo.

Vermote E., D. T., J.L. Deuze, M. Herman, J.J. Morcrette, and S.Y. Kotchenova, 2006, 6S User Guide Version 3.

Vincent, R. K., Qin, X., McKay, R. M. L., Miner, J., Czajkowski, K., Savino, J., and Bridgeman, T., 2004, Phycocyanin detection from LANDSAT TM data for mapping cyanobacterial blooms in Lake Erie: Remote Sensing of Environment, v. 89, no. 3, p. 381-392.

Wynne, T. T., Stumpf, R. P., Tomlinson, M. C., and Dyble, J., 2010, Characterizing a cyanobacterial bloom in western Lake Erie using satellite imagery and meteorological data: Limnology and Oceanography, v. 55, no. 5, p. 2025-2036.